ABSTRACT

Title of Thesis: CRYSTALLIZATION OF A SUBSURFACE OCEAN ON
                    TRITON

                    Jodi S Gaeman, Master of Science, 2011

Thesis directed by: Professor Saswata Hier-Majumder
                      Department of Geology

Planetary magma oceans are present throughout the Solar System in a variety of forms. Over time, these oceans pass through various evolutionary stages, influencing the dynamics of the planetary body in question. Magma ocean evolution is explored here in greater detail through a case study of a cryomagma ocean beneath the surface of Triton, Neptune's icy satellite. Triton is hypothesized to have experienced extensive tidal dissipation within its interior early during evolution. Given the influence of tidal dissipation, this study evaluates ocean sustainability using a parametrized turbulent convection model and a coupled crust-ocean evolution model. The latter model links the thermal evolution of the crust, solved as a Stefan problem, with the crystallizing multiphase ocean. Due to an evident 'tidal blanketing' effect, these models indicate that an ocean may survive around 1 billion years given Triton's present day orbit, a timescale that increases with increasing dissipation and orbital eccentricity.

CRYSTALLIZATION OF A SUBSURFACE OCEAN ON TRITON

by

Jodi S Gaeman

Thesis submitted to the Faculty of the Graduate School of the
University of Maryland, College Park in partial fulfillment
of the requirements for the degree of
Master of Science
2011

Advisory Committee:

Professor Saswata Hier-Majumder, Chair
Professor Daniel Lathrop
Dr. James Roberts

Acknowledgments

There are many people I would like to thank for their support throughout my graduate career. First, I would like to thank my advisor, Saswata Hier-Majumder, for all of his help and guidance over the years. Next, I would like to thank my Masters committee - James Roberts and Daniel Lathrop - for their assistance, input, and advice. I would also like to thank Laurent Montesi and Ved Lekic for their insightful comments and feedback.

Completing this thesis would not have been possible without the support of my family and friends, and the graduate students within the Geology Department, especially the geophysics group, namely Jesse Wimert, Jill Gribbin, Stephanie Johnston, Tyler Drombosky, Minjin Baek, and Kevin Miller. I am most grateful for their encouragement and motivation. Finally, I would like to thank Justin DeSha-Overcash for being the friendly and light-hearted individual he always was; both his playful distractions and committed focus served as much needed morale boosters. A welcomed addition to our lab group, his friendship and humor made my graduate experience all the more valuable to me.

Contents

List of Tables

List of Figures

Chapter 1

Background

1.1 Magma Oceans

Magma oceans are partially or completely molten bodies, occupying large fractions of planetary interiors. It has been hypothesized that magma oceans are likely to have existed at one time or reoccurringly throughout the history of many of our Solar System's planetary bodies. Evolution of magma oceans arise from a number of interrelated processes involving convective heat transfer, chemical composition, and tidal heating. So how do we characterize or classify a magma ocean?

Typically, we distinguish magma oceans according to their rheology, duration, size and shape, and composition. Rheologically, an ocean may be characterized through it's convective state. In general, an ocean's evolution is comprised of three main convective stages - "hard" turbulent convection stage, "soft" turbulent convection or soft ocean stage, and hard ocean stage (*Abe*, 1997; *Solomatov*, 2000). "Hard" turbulent convective stage occurs when the magma ocean has a very low viscosity, typically corresponding to a relatively high temperature for the composition of the system, and very vigorous convection associated with high Rayleigh numbers (*Shraiman and Siggia*, 1990; *Solomatov*, 2000). In many ways, this can be thought of as the initial stage of an ocean's evolution, occurring in conjunction with ocean formation. The convective vigor of this stage aids in removing excess heat from the ocean. The second stage, termed "soft" turbulence or soft ocean, exhibits similar features to that of "hard" turbulence in the sense that turbulent convection is still present due to the high melt fraction and low viscosity of the system. However, this stage is distinct from "hard" turbulence due to the reduced vigor of convection. Within a soft ocean, crystallization of solid can occur depending on the thermal state of the ocean, but it is unlikely to expect segregation of phases. Thus, solid particles are likely to remain suspended within the ocean, both phases having a distinct velocity (*Abe*, 1997; *Solomatov*, 2000; *Solomatov and Stevenson*, 1993a,b).

During the earliest stages of ocean evolution, turbulence aids in convecting away

2

a large amount of heat at the ocean's surface. Evolution, however, may also be influenced by the planetary body's tidal activity. In the case of an ocean residing beneath a crustal lid, it is possible that tidal heating can act to slow or counter ocean cooling. The influence of tidal activity is more significant for bodies with highly eccentric or inclined orbits. The stress induced during orbit contributes to a dissipation of heat within planetary bodies. *Roberts and Nimmo* (2008) show that the heating contributed from tidal deformation preferentially affects the ice shell as it is strongly dependent upon the rheology of the layer. However, significant tidal heating within the crust could aid in the formation of a new ocean, if not sustain a pre-existing subsurface one. As observations from Voyager, Galileo, and Cassini missions have shown evidence to suggest the presence of subsurface oceans in multiple icy satellites orbiting the outer solar system, tidal dissipation is expected to be a significant contribution to their presence (*Hussmann and Spohn*, 2004; *Hussmann et al.*, 2006; *Tobie et al.*, 2005).

1.2 Triton's Subsurface Icy Ocean

Overview

Triton is Neptune's largest moon with a radius of approximately 1353 km. Observations of the icy satellite's surface, shown in Figure 1.1, suggest evidence of recent geologic activity (*Prockter et al.*, 2005). The satellite's topography is marred by extensive ridge systems and volcanic plains. The eruptions of geysers and plume activity contribute to both the atmosphere and the landscape based on data collected from Voyager mission observations as well (*Brown and Kirk*, 1994; *McKinnon and Kirk*, 2007). The ages of many of the features documented remain unknown, however, the surface age of Triton is approximated between 10 and 100 Myr old (*Schenk and Zahnle*, 2007), which suggests relatively recent geologic activity. Internal heating of

Triton as a result of tidal dissipation may provide an explanation for this geologic activity at present. If substantial, *Ross and Schubert* (1990) show that tidal dissipation could explain the formation of an ocean within Triton using a basic parameterized coupled thermal-orbital evolution model. The presence of such a layer would be consistent with many of the surface observations of geologic and volcanic activity. Is there reason to suspect that an ocean might have been formed during Triton's history? If so, could the ocean have been sustained until present?

Geologic Activity on Triton

Knowledge of Triton is constrained by observations from the Voyager mission, based on images covering only about 40% of the satellite's surface. From this small sampling of the surface, three types of terrains can be distinguished - volcanic plains, polar caps, and dynamic "cantaloupe" terrain comprised of ellipsoidal depressions and ridges (*McKinnon and Kirk*, 2007). Overall, the topographic relief is limited to 1 km, though most features are significantly smaller (*McKinnon and Kirk*, 2007). Of the volcanic plains covering its surface, most indicate the extrusion of a viscous volcanic material, similar in nature to silicate flows, based on the extent of burial of the older topography (*Kargel*, 1995). This material would likely be comprised of a relatively ammonia-rich mix of an ammonia-water composition or a mix of ammonia, water, and methanol (*Kargel*, 1995; *McKinnon and Kirk*, 2007). Small caldera-like features are typically paired with the plains, likely serving as the origin for the cryovolcanic flooding (*Kargel*, 1995; *McKinnon and Kirk*, 2007). These broad, smooth volcanic plains represent one main variety of plains found on Triton.

Triton's surface also exhibits a second variety of volcanic plains referred to as walled and terraced plains (*Kargel*, 1995; *McKinnon and Kirk*, 2007). These plains are marked by some of the flattest terrain on Triton, suggesting the presence of fluid. More interesting is the relatively circular walls and terraces bounding the volcanism,
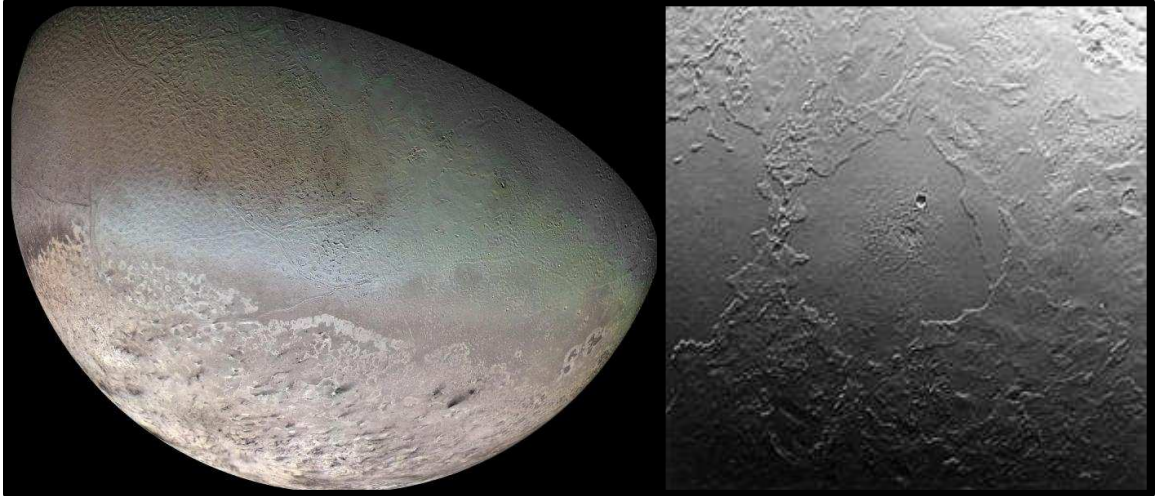
Figure 1.1: **Triton's Terrain** - These images of Triton were taken by the Voyager 2 spacecraft in 1989. The leftmost image shows the various terrains and geologic features of Triton, but most prominent is the "cantaloupe" terrain, named for its apparent similarity to a cantaloupe. This is best displayed in the top part of the picture. The rightmost picture shows one of the volcanic plains of Triton. The small circular depression in the center of the plain is thought to be a caldera. Images courtesy of NASA/JPL.

which have the appearance of being eroded by either wind or fluid. Overall, these plains represent the youngest terrain on Triton's surface (*McKinnon and Kirk*, 2007).

The oldest terrain on Triton is the "cantaloupe" terrain, depicted in Figure 1.1. The term "cantaloupe" is mainly attributed to the closely packed, 25-35 km elliptical depressions indicating diapiric activity likely due to compositional instability, or density stratification, in the crust. *Schenk and Jackson* (1993) estimate that the interaction between three layers of differing densities is necessary to explain the surface observations. One of their hypotheses suggests that an underlying low density crust could have been buried by volcanic deposits of increasingly denser substances. The overlying dense layers are approximated to be 20 km thick given the spacing of the depressions (*McKinnon and Kirk*, 2007; *Schenk and Jackson*, 1993). The terrain also hosts an intricate system of ridges, some similar to those on Europa, indicating extension or strike-slip faulting (*McKinnon and Kirk*, 2007; *Prockter et al.*, 2005). The third terrain, or the polar caps, are thought to be younger than the "cantaloupe"

terrain given partial burial of ridges around the pole regions. However, the coverage at the poles is not assumed to be thick. As such, this layer may serve as more of a glacier than true ice cap (*McKinnon and Kirk*, 2007).

Structure of Triton

From the data collected, the satellite is estimated to be approximately 1353 km in radius with an average density of approximately 2000 kg m^{-3} (*McKinnon and Kirk*, 2007). Models of the satellite's internal structure indicate that the satellite likely has a large silicate core, estimated to be approximately 1000 km radius, that is surrounded by icy layers. From limited observations, it is difficult to ascertain the structure of the icy portion of Triton. *McKinnon and Kirk* (2007) suggest that the satellite is differentiated given surface features indicative of melting and the distribution of various icy phases over the surface. Stratification is also likely given the evidence for diapirism at Triton's surface, suggesting that the outermost layer of Triton is denser than the ice beneath it (*McKinnon and Kirk*, 2007). A study by *Ruiz* (2003) suggests that the shell of Triton might only be approximately 20 km thick given the structure of some of the troughs assumed to be grabens observed by Voyager 2. *Ruiz* (2003) argues that depth of the trough should correspond to a discontinuity, which may be the brittle-ductile transition of the ice layer. Assuming this transition, the heat flow at the surface of Triton can be approximated for a purely conductive lid, and from that, the depth to a possible subsurface ocean. Of course, this makes many simplifying assumptions regarding heat flow, structure, and composition throughout the shell.

A very thin atmosphere of N$_2$ is also apparent from observations, including an approximately 8 km troposphere for weather (*Brown and Cruikshank*, 1997; *McKinnon and Kirk*, 2007). Plume activity is likely to contribute to the development of the atmosphere. As material is expelled, it becomes entrained by the wind and

transported across the surface (*Brown and Cruikshank*, 1997; *McKinnon and Kirk*, 2007). The resulting process is evidenced by the appeareance of streaks through the atmosphere extending a few 100 km in length and oriented east-west, and windtails at the satellite's surface. The appearance of these plumes is likely driven by solar heating rather than internal heating (*McKinnon and Kirk*, 2007). Heating causes sublimation of N_2 in the south, resulting in geysers. The N_2 is then transported and deposited in the north. The process also indicates large scale volatile transport across the satellite's surface that may correspond to seasonal variations (*Bauer et al.*, 2011; *McKinnon and Kirk*, 2007).

Orbital History

Triton likely began as a Kuiper Belt object and is hypothesized to have been captured into orbit about Neptune from an originally heliocentric orbit, likely prior to 4 Gyr (*Agnor and Hamilton*, 2006; *McKinnon and Kirk*, 2007; *McKinnon and Leith*, 1995). This hypothesis is based on the satellite's current orbital configuration, given its retrograde and inclined, circular orbit (*Agnor and Hamilton*, 2006). How the satellite was captured is not entirely clear. One hypothesis suggests that Triton was captured via binary-planet exchange, whereby Triton and a second body of similar size formed a binary system with the Sun (*Agnor and Hamilton*, 2006). As the binary's orbit approached Neptune, Triton was captured while the other body was tossed out of the system. Another, less favorable hypothesis suggests that the satellite may have been captured during a close encounter with Neptune, or a series of close encounters, causing a dissipation of orbital energy via gas drag (*McKinnon and Leith*, 1995). Once captured, Triton's orbit began to circularize from its highly elliptical state, evolving to its present condition with an eccentricity of 0.000016. At each passage of periapse, Neptune's gravity raised tides at the satellite's surface. The periodicity of this process dissipated energy within the satellite, reducing the energy of Triton's orbit

(*McKinnon and Kirk*, 2007). *Ross and Schubert* (1990) show that this circularization process occurred rapidly during the satellite's evolution. Deformation incurred by the satellite's orbital evolution would have dissipated a large amount of heat within Triton's interior, melting the icy layer of the satellite into a global ocean. *McKinnon and Kirk* (2007) approximate the dissipation of energy to be as much as 10^4 kJ kg^{-1}, enough to melt the satellite entirely.

Composition

Analysis of Voyager mission data has provided a glimpse of Triton's chemical constituents, but not a detailed analysis of its composition. Observations of surface features and spectral analysis have indicated that the satellite is predominantly H_2O with trace amounts of volatiles: N_2, CO, CO_2, and CH_4 (*Brown and Cruikshank*, 1997). Based on surface observations alone, about half of Triton's surface is composed of N_2 in solid solution with a minute amount of CO and CH_4. The other half is comprised of sections of either CO_2 or H_2O. These surface abundances, however, are not representative proportions of the satellite's interior (*Schenk and Jackson*, 1993). Models of presolar nebula chemical condensation lend an additional constraint to satellite composition. There is some variation amongst models, however, recent estimates suggest up to 15% ammonia within icy bodies in the outer Solar System (*Choukroun and Grasset*, 2010). The presence of a substantial amount of volatiles is significant in sustaining melt within an icy satellite as it decreases the temperature at which water may remain fluid (*Choukroun and Grasset*, 2010; *Croft et al.*, 1988; *Hogenboom et al.*, 1997). If an ocean on Triton formed approximately 4 Gyr ago, the presence of volatiles may contribute significantly to whether or not the ocean can have been sustained until present and influenced the structure of Triton's interior as well.

1.3　Objectives

Could an ocean, formed early during Triton's evolution, have been sustained until present within Triton's interior? To determine if an ocean has survived, it is necessary to explore ocean evolution in greater depth. The purpose of this study is to evaluate the crystallization of a cooling magma ocean and to understand the roles of varying influences throughout evolution, including tidal dissipation, multiphase dynamics, and composition. To this end, a coupled crust-ocean evolution model and a parametrized turbulent ocean evolution model are formulated to better understand ocean crystallization.

Chapter 2

Methodology

2.1 Governing Equations

Triton's thermal history can be studied in two steps. Shortly after binary capture and widespread melting of Triton's interior, the newly formed internal ocean of Triton convects in a turbulent manner. As this turbulent ocean cools and crystallizes, the average viscosity of its interior increases, while the inertial forces decline progressively. The transition between these two phases of thermal evolution takes place as a rheologically critical crystal fraction is reached (*Solomatov and Stevenson*, 1993a). We use a parametrized convection model for the turbulent regime and a two-phase flow model for the viscous flow regime in the interior of Triton. The equations governing each of these models are presented in the following subsections.

2.1.1 Parametrized Turbulent Convection

Thermal evolution of a convecting system is often described by parametrized convection models (*Schubert et al.*, 2000, Ch 13). In these models, the equation for energy conservation is integrated over the volume of the convecting system, resulting in an ordinary differential equation (ODE) in time for the average temperature T_{av} of the system,

$$mc_p\frac{\mathrm{d}T_{av}}{\mathrm{d}t} = -Aq \tag{2.1}$$

where m is mass of magma ocean, A is surface area, c_p is specific heat capacity, t is time, and q is the heat flux. The parametrization inherent to this group of models arises from a scaling relation between dimensionless numbers. In models of parametrized mantle convection, where inertial forces can be neglected, this scaling relation is a function of the dimensionless Rayleigh (Ra) and Nusselt (Nu) numbers. The dimensionless Rayleigh number, shown below, describes the convective vigor, while the Nusselt number represents the ratio between convective and conductive heat fluxes. For a turbulent system, however, the scaling involves the Prandtl (Pr)

number, which is the ratio of viscous to thermal diffusion. Using a scaling relation of *Shraiman and Siggia* (1990), the turbulent heat flux q through the ocean may be evaluated as:

$$q = 0.22k \left(\frac{T_{av} - T_s}{L} \right) \left(\frac{Ra^2}{Pr\lambda^3} \right)^{\frac{1}{7}} \tag{2.2}$$

where k is thermal conductivity, T_s is surface temperature, λ is aspect ratio, and L is thickness of the magma ocean. The nondimensional Prandtl and Rayleigh numbers are defined by,

$$Ra = \frac{\alpha g (T_{av} - T_s) L^3}{\kappa \nu}, \tag{2.3}$$

$$Pr = \frac{\nu}{\kappa}, \tag{2.4}$$

where α is the coefficient of thermal expansion, g is gravity, ν is the kinematic viscosity, and κ is the thermal diffusivity. Incorporating these equations for convective heat flux, the cooling rate term may now be rewritten as:

$$\frac{\mathrm{d}T_{av}}{\mathrm{d}t} = -\frac{0.22Ak}{Lmc_p} \left(\frac{Ra_0^2}{Pr\Delta T_0^2 \lambda^3} \right)^{\frac{1}{7}} (T_{av} - T_s)^{9/7}, \tag{2.5}$$

where ΔT_0 is a constant, reference temperature drop and Ra_0 is the Rayleigh number corresponding to ΔT_0. To track the evolution of the magma ocean's average internal temperature, we integrate the nonlinear ODE in equation (2.5) by using a fourth order, adaptive step-size, Runge-Kutta method (*Press et al.*, 1992).

The scaling relationship can vary depending on the degree and nature of viscous and thermal dissipation within the system, which is evaluated through the Prandtl and Rayleigh numbers. The Nusselt number is typically dependent upon the Rayleigh number such that:

$$Nu \sim Ra^{\gamma} \tag{2.6}$$

However, the γ coefficient for large Ra values in turbulent convection is not well defined. *Shraiman and Siggia* (1990) explored high Rayleigh number, hard turbulent convective systems in comparison to early experimental work on Helium and derived the scaling relationship to be:

$$Nu \sim 0.22 Ra^{\frac{2}{7}} Pr^{-\frac{1}{7}} \tag{2.7}$$

where γ is approximately 0.29. A more recent study by *Grossmann and Lohse* (2000) suggested a larger γ coefficient of approximately 0.43 or 0.33 depending on the characteristics of the system. The authors developed a general theory of 4 main regimes, divided based on relative Ra and Pr numbers. Given their classifications, two regimes are identified that could apply to Triton's turbulent ocean:

$$\text{for large } Pr : Nu \quad \sim \quad 0.00343 Ra^{\frac{3}{7}} Pr^{-\frac{1}{7}} \tag{2.8}$$

$$\text{for large } Ra : Nu \quad \sim \quad 0.038 Ra^{\frac{1}{3}} \tag{2.9}$$

Grossmann and Lohse (2011) further develop this unifying theory by focusing specifically on turbulent systems of $Ra \geq 10^{11}$, termed the ultimate regime. Experimental studies for Rayleigh values larger than 10^{11} yield a variety of γ coefficient values, most around 0.31, which is not unlike the coefficients supplied by *Shraiman and Siggia* (1990) or *Grossmann and Lohse* (2000). However, other experiments yield values around 0.38 or 0.25, which are vastly different (*Grossmann and Lohse*, 2011). *Grossmann and Lohse* (2011) suggest the variation depends upon the heat transport through the boundary layer and provide 3 possible scenarios to describe experimental values: plume thermal transport in a laminar boundary layer, background thermal

transport in a laminar boundary layer, or thermal transport in a turbulent boundary layer. The scaling relationship for the third scenario provides a substantially larger γ coefficient than what has been shown so far:

$$Nu \sim Ra^{\frac{1}{2}} Pr^{\frac{1}{2}} \tag{2.10}$$

A comparison of these scaling relationships is plotted in Figure 2.1. The relationships from *Shraiman and Siggia* (1990) and *Grossmann and Lohse* (2000) for large *Ra* appear to be the most comparable of the four shown. Aside from the regimes mentioned, *Grossmann and Lohse* (2011) emphasize that a combination of regimes can occur within a turbulent system as well. In that case, without greater understanding of the physical distinctions between each regime, any γ coefficient in the range of 0.14 to 0.39 could be feasible (*Grossmann and Lohse*, 2011). Because high Ra number scaling relationships remain uncertain, this model relies on equation (2.7) in the turbulent heat flux derivation for simplification (*Shraiman and Siggia*, 1990; *Solomatov*, 2007).

2.1.2 Coupled Crust-Ocean model

As Triton's ocean cools beyond the critical rheological transition, convective vigor diminishes to a viscous flow. Secular cooling of the satellite leads to continual freezing of the ocean and propagation of the icy crust from the surface towards the ocean-core boundary. Determination of the thermal structure in Triton's crust belongs to a class of problems, called the Stefan problems, that deal with describing the thermal profile within the frozen zone and calculating the freeze rate.. The schematic diagram in Figure 2.2 outlines the fundamental energy balance under this condition.

Consider the incremental growth of the crust over a small time period δt. As the ocean freezes to add the incremental layer, energy is released via the loss of latent heat of crystallization. Conservation of energy requires the latent heat of crystallization,

14
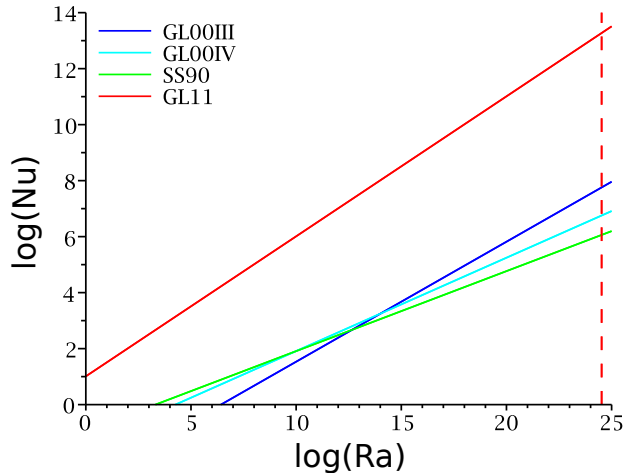
Figure 2.1: **Nu-Ra Scaling Relationships** - Four different scaling relationships are compared here for a turbulently convecting system. The dark and light blue lines represent two regimes described by *Grossmann and Lohse* (2000); green line represents the regime described by *Shraiman and Siggia* (1990); red line represents the scaling relationship of *Grossmann and Lohse* (2011). The dashed red line marks the approximate Ra value calculated for Tritons turbulent ocean within this model.

depicted as Q in the diagram, to be transported away from the freezing front by conduction. The efficiency of heat transport, therefore, limits the rate at which the freezing front propagates. Besides the conductivity of ice, latent heat and the presence of an additional heat source, such as tidal dissipation, is also likely to contribute to the rate of propagation of the freezing front. The following subsections outline the equations governing heat transfer within the advancing crust and the multiphase ocean.

Thermal evolution of the crust

In this section, we discuss the equation for energy conservation within the crust and the equation governing the thickness of the crust. As discussed above, we cast the problem as a Stefan problem with two unknowns, the crustal temperature $T_c(z, t)$, and the crustal thickness, $h(t)$. Conservation of energy within the crust leads to,
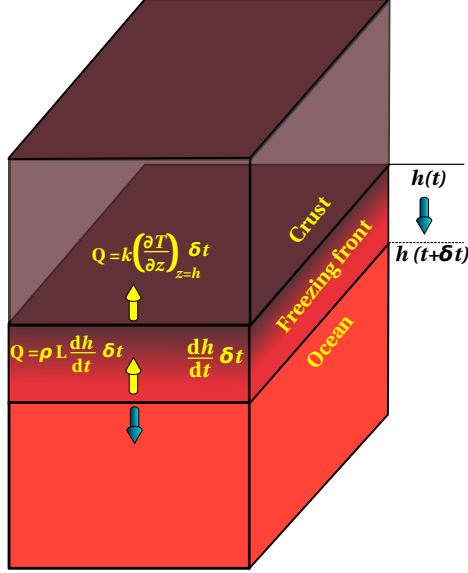
Figure 2.2: **Stefan Problem** - A schematic outline demonstrating the heat transfer in a crystallizing ocean, the Stefan problem. The freezing front advances by the amount $\left(\frac{\mathrm{d}h}{\mathrm{d}t}\right)\delta t$, over a small increment of time δt. The latent heat released by freezing must be conducted through the crust. The instantaneous position of the front is given by $h(t)$.

$$\frac{\partial T_c}{\partial t} = \frac{k}{\rho_c c_p}\frac{\partial^2 T_c}{\partial z^2} + \frac{\Psi_c}{\rho_c c_p}, \tag{2.11}$$

where T_c is temperature of the crust, t is time, $0 \leq z \leq h(t)$ is depth, ρ_c is the density, c_p is the specific heat capacity, k is the thermal conductivity, and Ψ_c is the volumetric tidal dissipation within the crust. All values for the constants can be found in Table 2.1. We assume that the crust is solid, implying a melt fraction of 0 throughout the entire layer.

We need an additional equation to solve for the unknown crustal thickness $h(t)$. This ordinary differential equation (ODE) arises from the balance between latent heat of crystallization and heat flux within the freezing front, as depicted in Figure 2.2, given by,

$$\frac{\mathrm{d}h}{\mathrm{d}t} = \frac{k}{\rho_c \Delta H}\left(\frac{\partial T_c}{\partial z}\right)_{z=h}. \tag{2.12}$$

The numerical solution building technique for this coupled system is discussed in

section 2.4.

Tidal dissipation throughout the crust is determined based upon the orbital state of the satellite and the rheological structure of Triton's interior. The formulations for tidal dissipation make use of the model presented by *Roberts and Nimmo* (2008). Subdividing Triton's interior into multiple layers distributed throughout the crust, ocean, and core, the spherical harmonic equations of motion governing displacement, stress, and potential (*Alterman et al.*, 1959) are solved using a propagator matrix method (*Sabadini and Vermeersen*, 2004) to determine a radial profile for tidal dissipation (*Roberts and Nimmo*, 2008; *Tobie et al.*, 2005). The equations and techniques governing the tidal dissipation parameter are better detailed in *Roberts and Nimmo* (2008).

Thermal and structural evolution of the multiphase ocean

The thermal evolution of the crust is coupled with the thermal evolution of a crystallizing ammonia dihydrate ocean layer. Though there are multiple processes to be explored within an ocean layer, here emphasis is placed on the influence from conduction, crystallization, and advection. Two-phase fluid dynamics are incorporated within this model to observe the effects of density variation between fluid and matrix phases and the role of crystallization throughout the layer. The equations used to describe this layer are derived from the mass, momentum, and energy equations following the model of *Sramek et al.* (2007).

As two phases - melt and matrix - are present, their masses are linked by melting and advection, given by the coupled partial differential equations,

$$\frac{\partial \phi}{\partial t} + \frac{\partial (\phi v_f)}{\partial z} = \frac{\Gamma}{\rho_f},$$ (2.13)

and

$$\frac{\partial (1 - \phi)}{\partial t} + \frac{\partial \left((1 - \phi) v_m \right)}{\partial z} = -\frac{\Gamma}{\rho_m},$$ (2.14)

Constants		(SI units)
α	Thermal Expansion Coefficient	5.0×10^{-5}
γ	Dimensionless Clapeyron Slope	$-\frac{\Delta S}{c_p}$
Γ	Melting Rate	$-\frac{\rho_m V}{H}$
Γ^*	Dimensionless Melting Rate	1.0
κ	Thermal Diffusivity	$\frac{k}{\rho c_p}$
λ	Aspect Ratio	1
ρ_c	Ice Shell Density - H_2O	917
ρ_f	Fluid Density	946
ρ_m	Matrix Density - H_2O	917
A	Surface Area	$4 \pi R^2$
c	Permeability Coefficient	1×10^{10}
c_p	Specific Heat Capacity	2096.7
g	Gravitational Acceleration	0.8
H	Length Scale	3.36×10^5
Δ H	Enthalpy of Fusion	1.32×10^5
k	Thermal Conductivity	2.0
L	Turbulent Ocean Thickness	3.36×10^5
m	Mass of Turbulent Ocean	$\frac{4}{3}\pi H^3 \rho_f$
R	Radius	1.353×10^6
Δ S	Entropy of Fusion	$\frac{\Delta H}{T_{fus}}$
t_0	Nondimensionalizing Time	5×10^{10}
T_0	Nondimensionalizing Temperature	240
T_{av0}	Nondimensionalizing Temperature	273
T_{fus}	Fusion Temperature	176
T_s	Surface Temperature	38
V	Nondimensionalizing Velocity	$\frac{k}{\rho_m c_p H}$

Table 2.1: **Table of Constants** - This table incorporates all constants and terms necessary to model Triton's interior.

Here, ϕ is the melt volume fraction, ρ_i and v_i are the density and velocity of each phase (for the melt $i = f$ and for the matrix $i = m$), and Γ is melting rate. Equations (2.13) and (2.14) represent the conservation of mass for the melt and the matrix, respectively. Since the densities of the two phases are different, the velocities of the melt and the matrix are also coupled by a momentum equation arising from the balance between buoyancy forces and percolation,

$$v_m - v_f = -\phi(1-\phi)\frac{(\rho_m - \rho_f)g}{c}, \tag{2.15}$$

where c is the frictional resistance to percolation. Notice that the work of *Sramek et al.* (2007) incorporates terms arising from matrix compaction in their coupled momentum conservation equations. Compaction of the matrix is crucial in expelling melt due to viscous deformation of matrix over characteristic length scales, termed compaction length. Typically, compaction length in a multiphase system is $O(\sqrt{\mu/c})$, where μ is the viscosity of the matrix. For the values $c = 1 \times 10^{10}$ Pasm^{-2} and $\mu = 10^{14}$ Pas, this length is ~ 100m, much smaller than the characteristic length scale of our problem. Therefore, we can avoid these negligible, second order terms for the current problem. Neglecting the compaction related terms also reduces the governing PDEs to first order in velocities and melt fraction.

Finally, the temperature distribution within the ocean is given by the multiphase adiabatic gradient

$$\frac{\mathrm{d}T_m}{\mathrm{d}z} = \frac{\alpha' g T_m}{c_p'} \tag{2.16}$$

where c_p' is the effective heat capacity, g is gravity, and α' is the effective coefficient of thermal expansion. The effective quantities can be determined from the end member

compositions using the relations,

$$\alpha' = \alpha + \frac{\Delta\rho}{\rho(T_{liq} - T_{sol})}, \qquad (2.17)$$

$$c_p' = c_p + \frac{\Delta H}{\rho(T_{liq} - T_{sol})}, \qquad (2.18)$$

where ΔH is the enthalpy of fusion (*Solomatov*, 2007). Once the thickness of the crust is calculated, we calculate the thermal profile within the ocean using the adiabatic gradient given in equation (2.16).

2.2 Nondimensionalization

2.2.1 Parametrized Turbulent Convection

The parametrized turbulent convection model is nondimensionalized by:

$$T_{av} = T_{av}^* T_{av0}$$

$$t = t^* t_0$$

Using this nondimensionalization scheme, but dropping the * notation, the governing equation becomes:

$$\frac{dT_{av}}{dt} = -\frac{0.22 A k t_0}{L m c_p} \left(\frac{Ra_0^2 T_{av0}^2}{Pr \Delta T_0^2 \lambda^3} \right)^{\frac{1}{7}} \left(T_{av} - \frac{T_s}{T_{av0}} \right)^{9/7}, \qquad (2.19)$$

As the cooling rate of Triton's turbulent ocean, equation 2.19 evaluates the evolution of the average temperature of the satellite assuming rapid, turbulent convection of heat lost at the surface of the satellite, from a global ocean extending the depth to Triton's core. As the turbulent ocean cools, it is expected that crystallization begins as temperature drops below the liquidus of the system. Turbulent convection

20

continues, however, until a critical rheological transition is attained. This transition is associated with a drastic increase in viscosity, which ultimately prevents turbulent convection from continuing due to the large crystal fraction within the ocean. This marks the transition to the icy ocean's viscous flow stage, and the transition to the coupled crust-ocean evolution model.

2.2.2 Coupled Crust-Ocean Evolution

As the equations describing the multiphase ocean's evolution are mainly based on the work of *Sramek et al.* (2007), the nondimensionalization of this model is derived similarly. All terms containing an * are the nondimensional form of those without. Ideally, temperature provides the scaling for this system, ranging from 0 to 1, where 1 is the equivalent to the liquidus of the system and 0 is approximating surface temperature. Based on this scaling

$$T = T^*T_0$$

$$z = z^*H$$

$$v_i = v_i^* \frac{k}{\rho_m c_p H}$$

$$\Gamma = \Gamma^* \frac{\rho_m V}{H}$$

$$\Psi_c = \frac{kT_0}{H^2} \Psi^*$$

dropping asterisks from the dimensionless variables, the final dimensionless governing equations become:

$$\frac{\partial T_c}{\partial t} = \frac{\partial^2 T_c}{\partial z^2} + \Psi_c \tag{2.20}$$

$$\frac{\mathrm{d}h}{\mathrm{d}t} = St \left(\frac{\partial T_c}{\partial z} \right)_{z=h} \tag{2.21}$$

$$\frac{\partial \phi}{\partial t} = \Gamma + \frac{\partial \left((1-\phi)v_m \right)}{\partial z}, \tag{2.22}$$

$$\frac{\partial}{\partial z} \left(\phi v_f + (1-\phi)v_m \right) = \frac{\Gamma(\rho_m - \rho_f)}{\rho_f}, \tag{2.23}$$

$$v_m - v_f = -\beta\phi(1-\phi), \tag{2.24}$$

We obtain equation (2.23) by eliminating the time derivative between the two mass conservation equations. The system of five coupled equations (2.20) - (2.24), are solved for the five unknown variables: T_c, v_m, v_f, ϕ and h. Three nondimensional quantities govern the behavior of the system. The first quantity, the Stefan number, given by

$$St = \frac{T_0 c_p}{\Delta H}, \tag{2.25}$$

signifies the ratio between the efficiency of heat transfer by conduction and heat generation by freezing. As seen from equation (2.21), the freeze rate $\mathrm{d}h/\mathrm{d}t$ is directly proportional to St. Using the values listed in table 2.1, we obtain $St = 2.79$, which was used in our numerical simulations. The next dimensionless number β is given by the ratio between buoyancy and frictional resistance to percolation,

$$\beta = \left(\frac{(\rho_m - \rho_f)g}{c} \right) \left(\frac{\rho_m c_p H}{k} \right), \tag{2.26}$$

where the second quantity within parentheses on the right hand side is the inverse velocity scale for the problem. This velocity scaling arises from the ratio between the characteristic length scale and thermal diffusive time. Using the values considered in this work, we obtain $\beta = -749.38$. Finally, the third dimensionless quantity γ is the

dimensionless Clapeyron slope of melting, given by,

$$\gamma = \frac{\Delta s}{c_p}. \tag{2.27}$$

Based on the constants listed in Table 2.1, we use $\gamma = 0.36$.

2.3   Initial and Boundary Conditions

2.3.1   Parametrized Turbulent Convection

The parametrized turbulent convection model evaluates Triton's early evolution using a turbulent convective cooling rate that assumes cooling from an initial superliquidus temperature. The initial temperature prescribed for this study is approximately 273 K. The solved cooling history prescribed by this parametrized model, in turn, translates to the upper boundary condition required to evaluate an evolving adiabat within a crystallizing turbulent ocean.

2.3.2   Coupled Crust-Ocean Evolution

The coupled crust-ocean evolution is governed by the system of five equations described by (2.20)-(2.24). The energy equation is second order in z and first order in t. Thus, we need to specify two boundary conditions and an initial condition for the temperature field. The relevant boundary conditions are displayed in Figure 2.3. These boundary conditions are given below,

$$T_c(0,t) = T_{surf} \tag{2.28}$$

$$T_c(h(t),t) = T_{sol} \tag{2.29}$$

$$T_c(z,0) = 0 \tag{2.30}$$

23

The initial condition for crustal thickness h is given by,

$$h(0) = 0. \tag{2.31}$$

We require an initial condition and a boundary condition for the melt fraction and one boundary condition for each velocity, given by,

$$
\begin{align}
\phi(z, 0) &= \frac{T_m(z, 0) - T_{sol}}{T_{liq} - T_{sol}}, \tag{2.32}\\
\phi(0, t) &= 0, \tag{2.33}\\
v_m(0, t) &= 0, \tag{2.34}\\
v_f(0, t) &= 0. \tag{2.35}
\end{align}
$$

The schematic diagram in Figure 2.3 outlines some of these boundary conditions with respect to Triton's interior.

2.4   Numerical Techniques

In this model, thickness of the conductive crust grows with time, while the ocean shrinks by freezing. The nature of the moving boundary in the problem requires special attention to a few details. First, the moving boundary leads to adaptive remeshing in order to keep the model resolution reasonable. Secondly, the freeze rate in equation (2.21) becomes near zero if the initial crustal thickness and initial crustal heat flux are both small or near zero (*Mitchell and Vynnycky*, 2009). To address both of these issues, we employed the Boundary Immobilization Method (BIM) (*Caldwell and Kwan*, 2004; *Mitchell and Vynnycky*, 2009). In the adaptive BIM, we make the substitution,
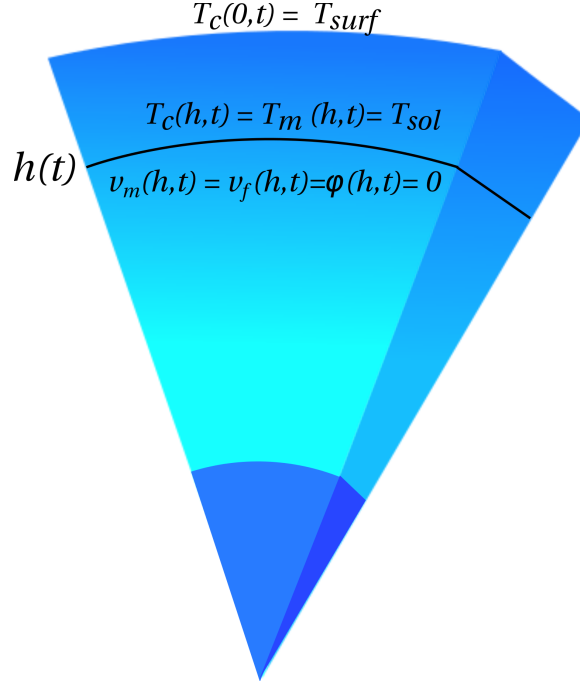
Figure 2.3: **Boundary Conditions** - Boundary conditions for the temperatures, melt fractions, and velocities in Triton's interior. In the dimensionless scheme, we set $T_{surf} = 0$, and $T_{sol} = 0.73$.

$$z' = \frac{z}{h},\tag{2.36}$$

to solve equations (2.20) and (2.21). After making the substitution, equations (2.20) and (2.21) can be rewritten in terms of a new function $f(t) = h^2$,

$$f\frac{\partial T_c}{\partial t} = \frac{z'}{2}\frac{\mathrm{d}f}{\mathrm{d}t}\frac{\partial T_c}{\partial z'} + \frac{\partial^2 T_c}{\partial z'^2} + f\psi\tag{2.37}$$

$$\frac{\mathrm{d}f}{\mathrm{d}t} = 2\alpha\left(\frac{\partial T_c}{\partial z'}\right)_{z'=1}.\tag{2.38}$$

Following the technique outlined by *Mitchell and Vynnycky* (2009), we discretize equations (2.37) and (2.38) implicitly in temperature and explicitly in crustal thickness. The discretized equations can be written as,

25

$$f^n \left(T_i^n + \psi_i^n\right) = -\frac{\Delta t}{\Delta z^2} \left[\frac{\Delta z}{4} z' \left(\frac{\mathrm{d}f}{\mathrm{d}t}\right)^n + 1\right] T_{i+1}^{n+1}$$
$$\frac{\Delta t}{\Delta z^2} \left[\frac{\Delta z}{4} z' \left(\frac{\mathrm{d}f}{\mathrm{d}t}\right)^n - 1\right] T_{i-1}^{n+1} + \left[\frac{2\Delta t}{\Delta z^2} + f^n\right] T_i^{n+1} \quad (2.39)$$

$$f^{n+1} = f^n + \frac{\alpha \Delta t}{\Delta z} \left[3T_M^n - 4T_{M-1}^n + T_{M-2}^n\right]. \quad (2.40)$$

The first discretized equation leads to a tridiagonal system of linear equations, which was solved using subroutines from LAPACK library implemented via the intel Math Kernel Library. We also tested the sample problem of freezing of a planar interface discussed by *Mitchell and Vynnycky* (2009) and *Caldwell and Kwan* (2004) to benchmark our results. The results for this benchmark are provided in the appendix.

Chapter 3

Results

3.1 Triton's Subsurface Icy Ocean

Ultimately, the objective of this study is to ascertain whether an ocean may still be present within Triton today. To address this goal, it is necessary to evaluate the combined duration of both the turbulent and multiphase ocean stages of Triton's evolution.

3.1.1 Thermal Evolution of Turbulent Ocean

The parametrized turbulent ocean model considers the evolution of Triton's ocean throughout the earliest stage of cooling after ocean formation, when the ocean is entirely molten and beginning to crystallize. As shown in figure 3.1, this stage of crystallization occurs very rapidly. In less than 1000 yrs, the ocean has already transitioned from turbulent ocean dynamics to multiphase ocean dynamics. It is important to note, however, that the parameters influencing this model remain constant with time. The thermodynamic parameters used to calculate this cooling rate exhibit no change as crystallization occurs.
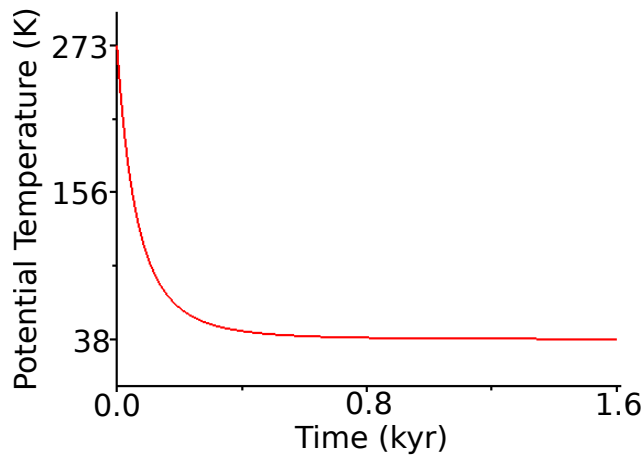
Figure 3.1: **Cooling Rate for Turbulent Global Ocean** - The cooling rate shown here is the evolution of the average temperature of the ocean. Temperature cools rapidly due to turbulent convection.
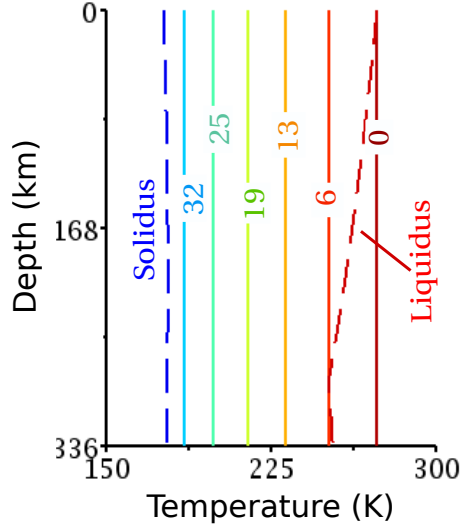
Figure 3.2: **Evolution of Turbulent Ocean Adiabats** - Plot of a series of adiabatic thermal profiles within the turbulent magma ocean. The solidus (*Hogenboom et al.*, 1997) and liquidus (*Choukroun and Grasset*, 2007) temperatures, drawn in broken curve, are displayed in the plot. Annotations on the adiabatic temperature profiles indicate the number of years since the beginning of the simulation.

The interior of the ocean exhibits a steep adiabatic temperature gradient. Consequently, the entire ocean cools evenly with the rapid drop in the potential temperature. The series of plots in Figure 3.2 displays the evolution of the ocean's interior during this period. The numbers on the plot indicate number of years since the commencement of the cooling, roughly coincident with the end of Triton's circularization. As the plots indicate, Triton's turbulent cooling phase likely lasted for only a few decades. Notice that early in the history of turbulent cooling, the adiabat intersects the liquidus near the top of the ocean, marking the site of the first crystallization.

3.1.2   Coupled Crust-Ocean Model

As the rapid turbulent cooling of Triton leads to the crust formation, a number of factors begin influencing the rate of cooling. The two most important factors during this phase are tidal dissipation within the crust and conductive heat loss through the crust. The following subsections outline the results from our simulations illustrating

29

the nature of interplay between these coupled processes.

Tidal Dissipation Within the Crust

As the high viscosity crust forms atop the magma ocean, tidal dissipation within the crust increases the temperature. Two important features of the tidal dissipation are displayed in the plots in Figure 3.3. First, the profile in Figure 3.3, demonstrates the vertical distribution of tidal heating within the crust. In this plot, the crust is 168 km thick. As the plot indicates, tidal dissipation within the ocean is negligible compared to the dissipation within the crust. The ocean decouples the crust from the core, concentrating heating near the base of the crust. Since tidal dissipation preferentially warms the bottom of the crust, freezing and crust growth at the crust-ocean boundary is impeded.

Second, the magnitude of tidal dissipation near the bottom increases nonlinearly with an increase in the eccentricity. The series of thermal profiles in Figure 3.3(b) demonstrate this effect. By increasing the orbital eccentricity by a factor of 3, tidal heating has been increased by over an order of magnitude. Taken together, these two factors prevent the ocean within a satellite in an eccentric orbit from losing heat by a blanketing effect. The importance of this effect becomes clear when we consider the interplay between tidal heating and crust propagation, discussed next.

Thermal and Structural Evolution

In this section, we present the evolution of Triton's thermal and structural profile for a series of different orbital eccentricities. The plots in Figure 3.4 depict the thermal profile and tidal heating at three different time steps. The plots in Figure 3.4(a) and (c) correspond to an orbital eccentricity of 1×10^{-2} and 6×10^{-3} respectively. The legends on the curves indicate time in million years since the crystallization of the crust started. In a sharp contrast to the turbulent cooling phase, large parts of the
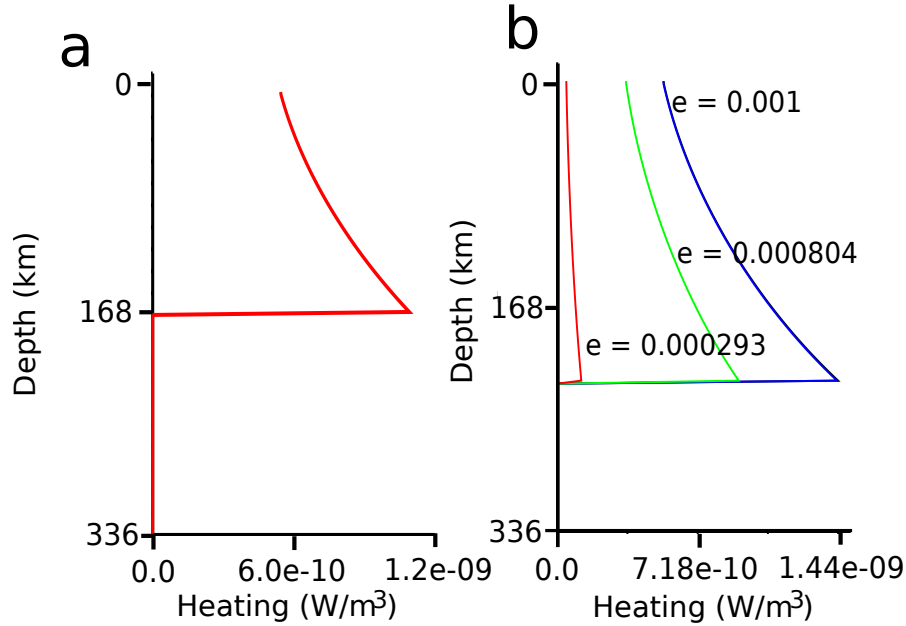
Figure 3.3: **Crustal Heating Profile** - (a)This is a sample plot of a typical crustal heating profile for a given depth. Within the crust, maximum dissipation occurs at the base. Within the ocean, heating is negligible. Heating output is in W/m^3. (b)Tidal dissipation profiles are plotted for three different eccentricities according to how Triton's orbit evolves within this model. Dissipation is shown to increase with increasing eccentricity.

satellite's interior remain molten even after 3.4 billion years. The relatively high eccentricity in these test cases are higher than Triton's current eccentricity, but such eccentric orbits must have existed in Triton's past assuming a capture origin. The steep adiabatic gradient within the ocean, to the right of the broken vertical line, indicates that the temperature of the nearly isothermal ocean is not substantially higher than the solidus. With the passage of time, the maximum amount of tidal heating near the bottom of the crust remains the same for both cases.

Secular cooling and growth of the crust are more pronounced at lower orbital eccentricities. A similar series of plots in Figure 3.5, compare the thermal and tidal dissipation profile at three different time steps for orbital eccentricities of 1×10^{-5} and 2×10^{-3}, respectively. In both of these cases, the crust grew to almost 250 km thickness. The time required for the crustal growth, over 1 billion years, is markedly

different from the turbulent cooling phase. The slow, sustained growth of the crust is impeded by a weak, yet effective tidal warming.

Numerical solutions to the Stefan problem allow us to calculate the growth and growth rate of Triton's crust as a function of time for different eccentricities. The results from these simulations are plotted in Figures 3.6(a) and (b). The plot in Figure 3.6(a) also overlays the current estimate of the depth to Triton's core. The legends on the plots indicate orbital eccentricity. Of the range of orbital eccentricities explored in this work, the current orbital eccentricity of 1×10^{-5} is able to prevent complete freezing of Triton's interior for over a period of 1.5 billion years. For orbital eccentricities higher than 2×10^{-3}, part of the interior of the satellite remains melted. The plots in Figure 3.6(b) also indicate that within the first 500 million years, the freeze rate $\mathrm{d}h/\mathrm{d}t$, reduces to less than half the original value. The freeze rate falls more sharply for higher orbital eccentricities.

From the numerical simulations we evaluate the surface heat flux and the heat flux at the base of the crust as a function of time for various values of orbital eccentricity in Figure 3.7. Comparison between these two plots, and different curves within each plots demonstrate the tidal blanket effect. First, the heat flux near the surface is higher than the basal heat flux. Moreover, the basal heat flux decreases faster with time for higher eccentricity orbits. As demonstrated in Figure 3.3 and the series of heating profiles in Figures 3.4 and 3.5, the base of the crust is preferentially warmed by tidal heating, while the surface is kept at a low temperature, leading to a lower basal heat flux. Secondly, the magnitude of tidal blanketing increases with higher eccentricity orbits, reducing the basal heat flux. As evidenced from equation (2.21), the growth rate of the crust is directly proportional to the basal heat flux. Thus, reducing the basal heat flux by concentrating tidal heating near the bottom slows down the rate of crustal growth.
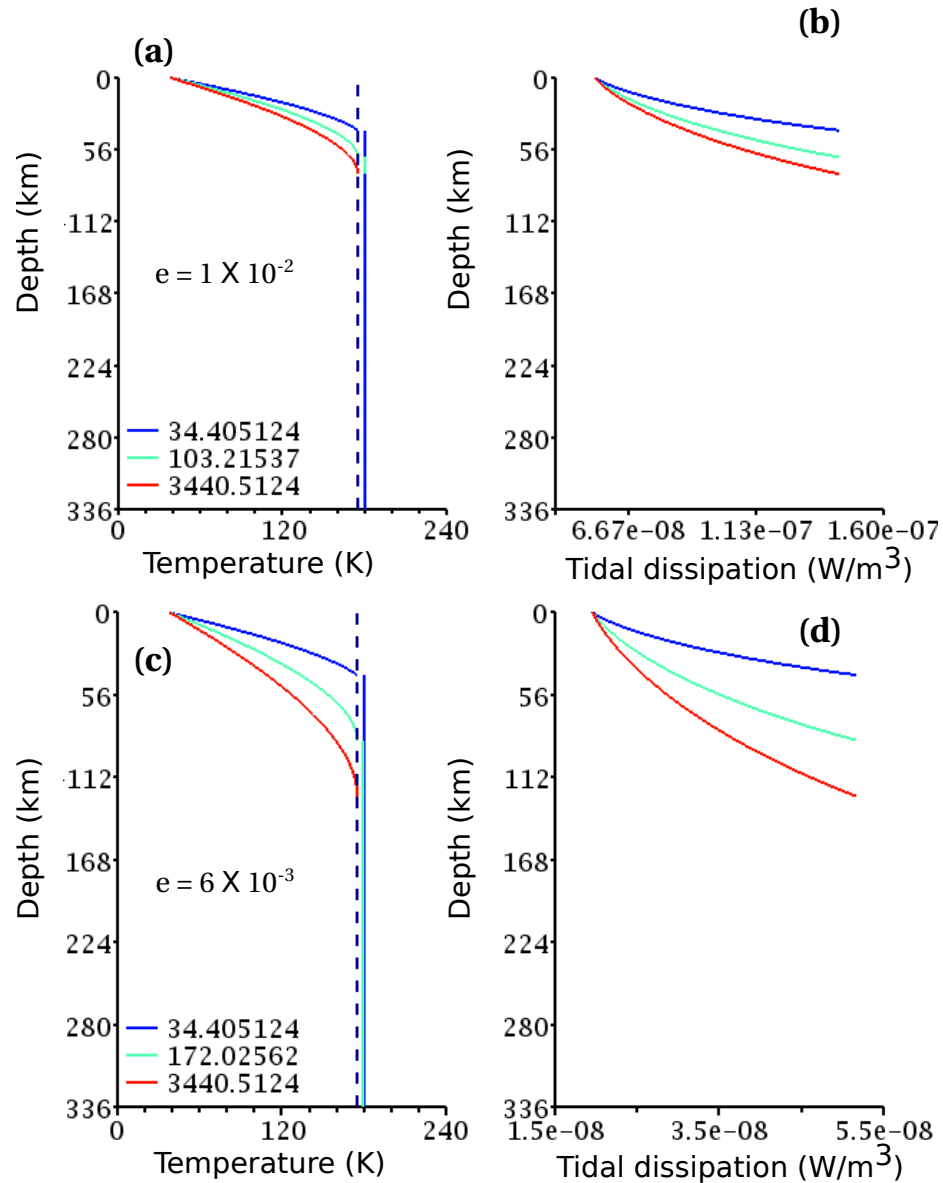
Figure 3.4: **Crust-Ocean Evolution for Larger Eccentricities** - Profiles of crustal temperature (a,c) and heating as a function of depth (b,d). The legends on the curves indicate time in million years. The vertical broken line indicates the near surface solidus temperature.
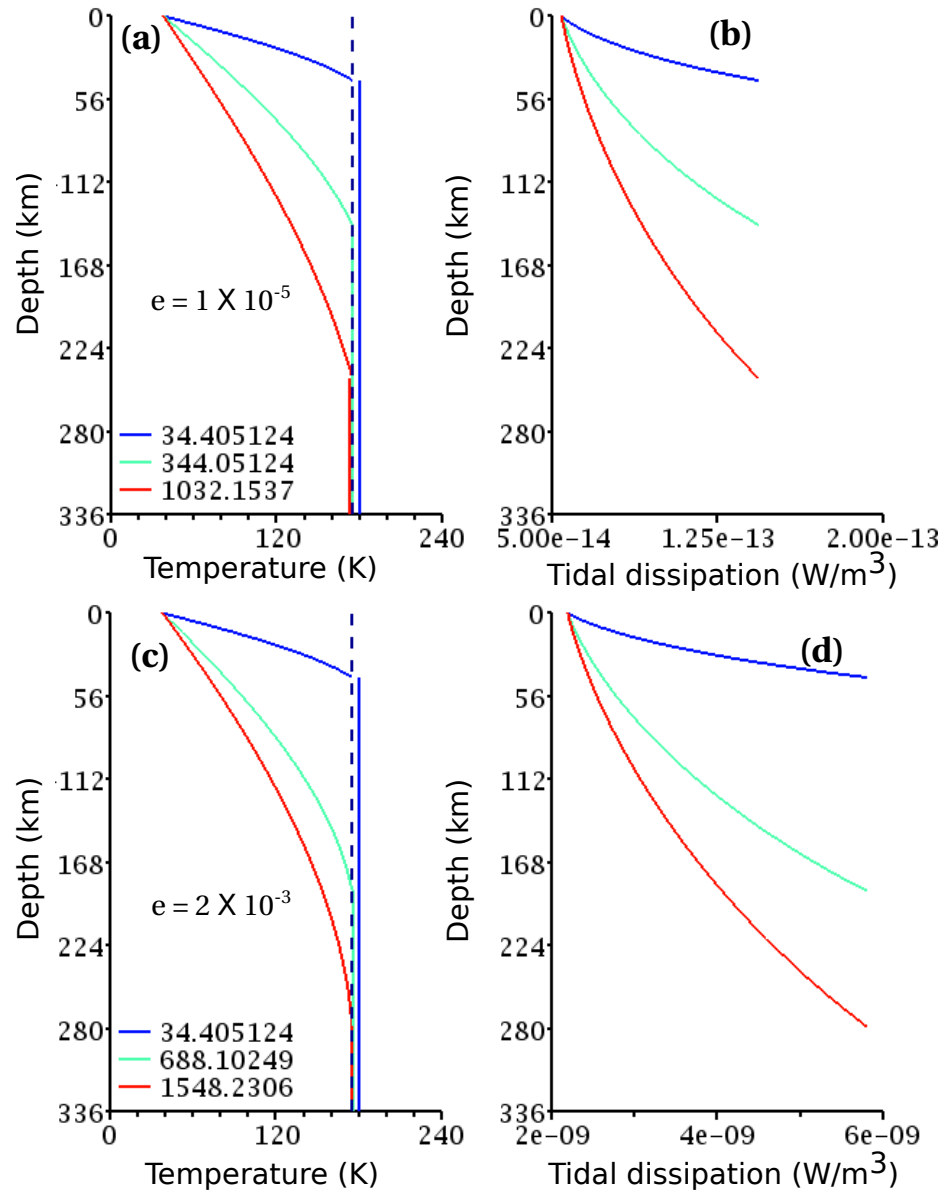
Figure 3.5: **Crust-Ocean Evolution for Smaller Eccentricities** - Profiles of crustal temperature (a,c) and heating as a function of depth (b,d). The legends on the curves indicate time in million years. The vertical broken line indicates the near surface solidus temperature.
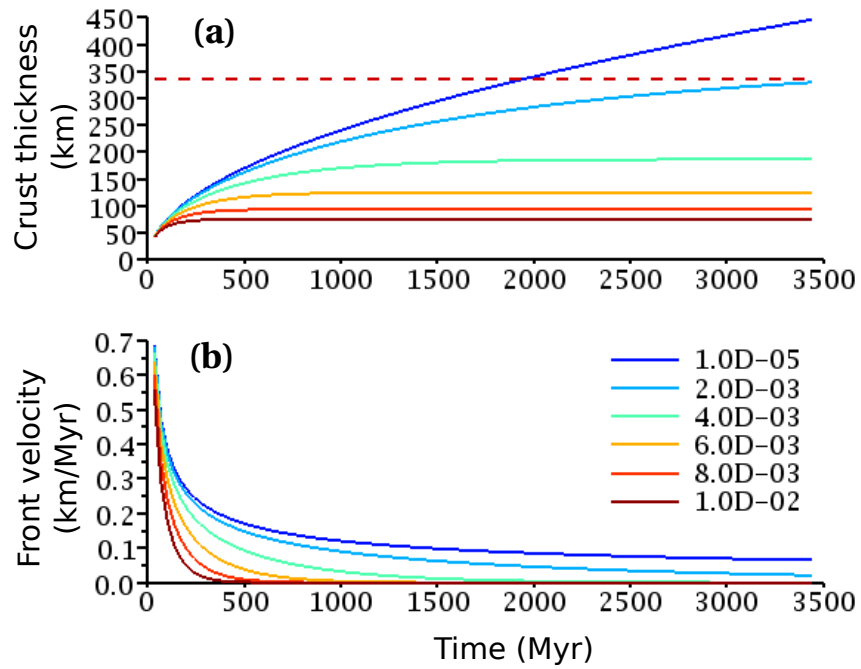
Figure 3.6: **Freezing rate of the magma ocean**- (a) Thickness of the icy crust in km, and (b) velocity of the freezing front as a function of time in million years. The legends on the plots correspond to different values of orbital eccentricity. The broken horizontal line in (a) represents the current estimate of the depth to the core.
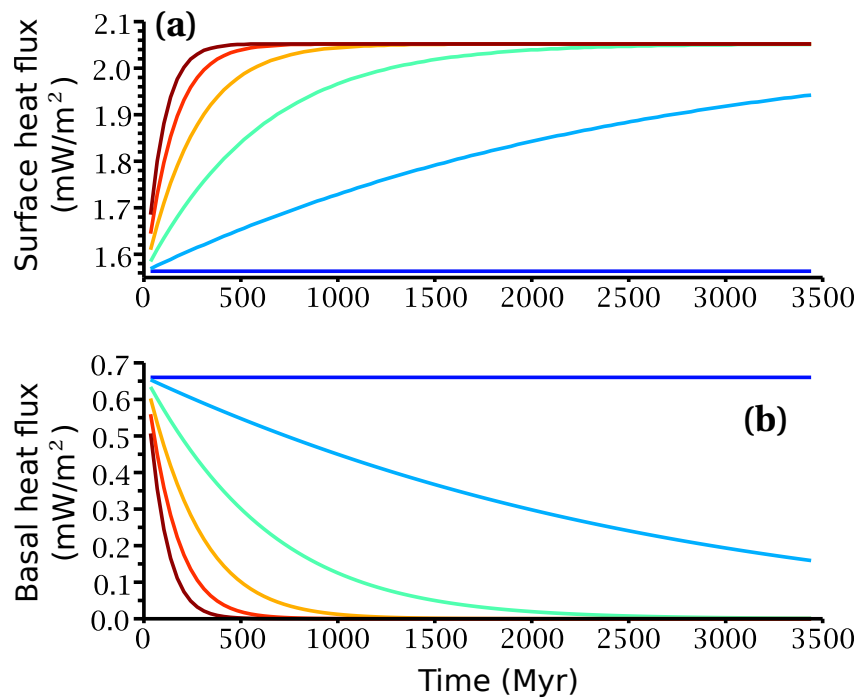
Figure 3.7: **Crust-Ocean Heat Flux** - Normalized (a) surface and (b) basal heat flux in the freezing crust as a function of time. Different curves on the plot correspond to different orbital eccentricities. The legends, omitted to avoid cluttering, are identical to those in Figure 3.6(b).

Chapter 4

Discussion
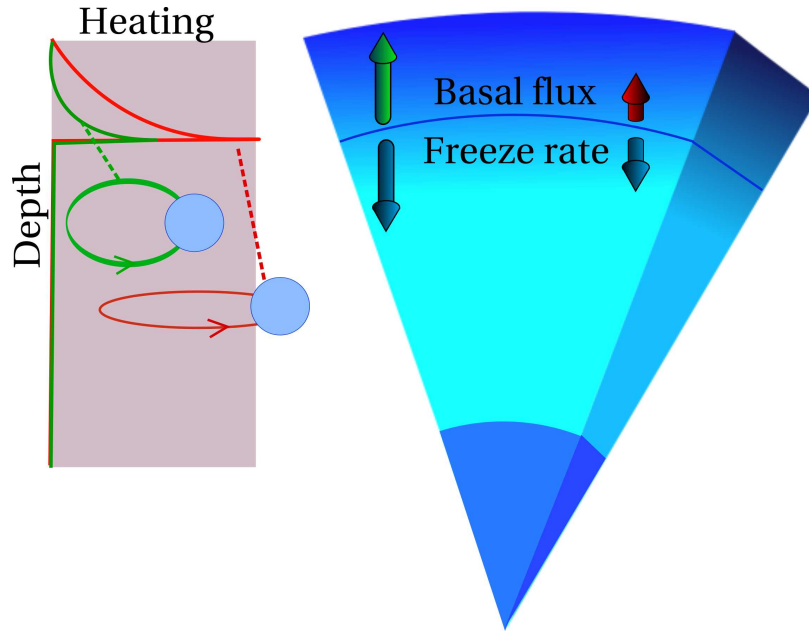
Figure 4.1: **Tidal Blanket Effect** - A schematic diagram outlining the tidal blanketing effect in the crystallizing crust. Lengths of the upward pointing red and green arrows correspond to the magnitudes of basal heat flux arising from the tidal dissipation. Similarly, lengths of the downward pointing blue arrows represnt the magnitudes of crustal growth for the two cases. As indicated in the cartoon, higher tidal dissipation corresponds to lower basal heat flux and a reduced rate of crustal growth.

4.1   Tidal blanketing

Tidal dissipation in the growing crust insulates the underlying, crystallizing ocean, reducing the basal heat flux and delaying crustal growth. The overall effect of a highly dissipative crust is to provide a thermal blanket atop the ocean. We term this the 'tidal blanketing' effect. The cartoon in Figure 4.1 summarizes some of the key processes associated with tidal blanketing. First, we notice that tidal dissipation is typically concentrated near the base of the crust. The concentration of tidal heating near the base arises from mechanical decoupling between the crust and the ocean. Next, we notice that the growth rate of the crust, derived from the Stefan problem, is proportional to the basal heat flux. Since the base of the crust is fixed at the solidus temperature, warming of the lower part by tidal dissipation reduces the

thermal gradient and thus the basal heat flux. Consequently, the growth of crust by crystallization is impedded. Since high eccentricity of the orbit leads to larger tidal dissipation, the tidal blanketing effect is stronger at higher eccentricites.

4.2 Compositional complexities

Composition of the satellite is necessarily simplified to an NH_3-H_2O system in many icy satellite studies. Here, this system is further simplified through our thermodynamic model, which ignores the depth dependence of thermodynamic parameters. The solidus is taken to be constant with depth, which is shown in Figure 3.2 to be a reasonable approximation. The liquidus temperature, however, does change with depth and may not necessarily correspond to the H_2O solidus as assumed here. It would be interesting to incorporate this depth dependence within this evolutionary model.

Overall, the liquidus of this system depresses with increasing pressure. This trend reverses at pressures of 300 MPa (*Hogenboom et al.*, 1997). As *Hogenboom et al.* (1997) discuss, the density of NH_3-H_2O liquid remains lighter than that of solid ammonia dihydrate I up until 160 MPa. Between 160 and 300 MPa, the liquid becomes denser than the solid phase. Beyond 300 MPa, the system no longer crystallizes ammonia dihydrate I, but switches to ammonia dihydrate II, corresponding to the reversal in the liquidus depression trend (*Hogenboom et al.*, 1997). Within Triton, the base of this NH_3-H_2O layer should extend well into the pressure range for the denser liquid. In fact, this dynamic may provide one possible method of obtaining a basal ocean (*Fortes et al.*, 2003; *Hogenboom et al.*, 1997). Keeping in mind that tidal dissipation is most influential within a crust decoupled from a core (*Roberts and Nimmo*, 2008), it would be interesting to add this transition to this model. These effects may have several implications for ocean life extension and volcanism on icy
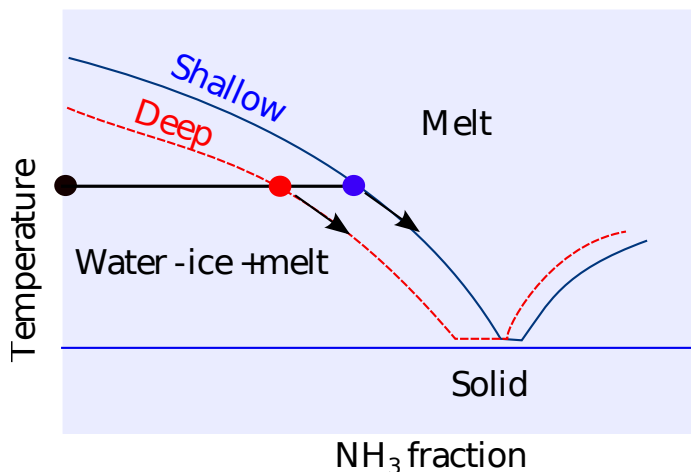
Figure 4.2: **Ammonia-Water Composition** - A schematic melting diagram in the NH_3 - H_2O system, modified from (*Hogenboom et al.*, 1997). The red and blue dots indicate the composition of a magma in equilibrium with an H_2O-ice phase at deep and shallow levels, respectively.

satellites as well.

The other compositional simplification we make, related to the previous, is that bulk fluid composition and density remain constant over time as crystallization occurs. Depending on the dynamics of the system, if grains crystallizing from the initial fluid are concentrated in one particular component and then segregated out of the system, the fluid density should evolve correspondingly, altering the liquidus and solidus of the system. This may have an impact on the sustainability of the ocean.

4.3 Composition of Magma Oceans

One consequence of crystallization of the magma ocean is progressive change in the composition of the magma. As illustrated in the cartoon in Figure 4.2, the concentration of ammonia within the magma ocean increases with progressive crystallization. Since the crust of Triton is predominantly composed of water-ice, it is likely that the bulk composition lies on the H_2O side of the eutectic curve in Figure 4.2. As the ocean cools and crystallization progresses, composition of the liquid evolves along the

liquidus curves, in the direction indicated by the arrows in the diagram. One important consequence of such progressive enrichment of the ocean in NH_3 is that the liquid becomes denser than the crystallizing H_2O-ice (*Hogenboom et al.*, 1997). Progressive enrichment of the liquid in NH_3 also reduces its viscosity (*Hogenboom et al.*, 1997), enhancing gravitational drainage of trapped pore fluid within the freezing front. As a consequence, a thin layer of NH_3-rich magma can be rendered dynamically stable beneath the ice shell. Although the liquidus is shifted towards the H_2O end of the phase diagram at higher pressures, the trend of compositional enrichment still exists. Thus with sufficient tidal blanketing, it is possible to create an NH_3-rich magma layer at the base of the crust.

Chapter 5

Conclusion

This simplified coupled crust-ocean model provides a first look at the interplay between various icy satellite dynamics, which can greatly alter the evolution of a satellite's interior and possibly exterior. Though simplified, it suggests that an ocean may exist at present due to the large influence tidal dissipation may have within the crust, namely this 'tidal blanketing' effect. It is worth evaluating the scenario further to gain a better approximation for the duration of an ocean as well as the extent and characteristics of the ocean to determine whether it may be contributing to surface activity at present and by what means. Further evaluation and analysis of some of the assumptions made here may aid in explaining volcanism and tectonic activity on several icy satellites throughout the solar system. Likewise, this model may be applied to the evolution of silicate bodies as well. Future studies should consider the role of composition, tidal dynamics, and two phase flow dynamics more extensively for a better approximation of ocean endurance.

Appendix A

Coupled Crust-Ocean Model

A.1   Steady State Analytical Solution

Equations (2.13) and (2.14) can be used to derive a steady state analytical solution for the velocities of each phase in the multiphase ocean model. Motion of each phase results from the variation in density between melt and crystals. The percolation of melt through the matrix influences the advection of heat throughout the multiphase layer. To determine the velocity of each phase, we can begin by subtracting equation (2.14) from equation (2.13):

$$-\frac{1}{\rho_m - \rho_f}\left(\frac{\partial \phi}{\partial z}v_m - \frac{\partial v_m}{\partial z} + \frac{\partial v_m}{\partial z}\phi - \frac{\partial \phi}{\partial z}v_f - \phi\frac{\partial v_f}{\partial z}\right) - \frac{\Gamma}{\rho_f \rho_m} = 0, \qquad (A.1)$$

This equation can then be integrated with respect to z. We impose a boundary condition on the velocities such that $(1 - \phi)v_m + \phi v_f = 0$ at z = 0. Thus, the average velocity of the system is 0 at $z{=}0$. Equation (A.1) becomes

$$0 = \frac{1}{\rho_m - \rho_f}((1 - \phi)v_m + \phi v_f) - \frac{\Gamma z}{\rho_f \rho_m}, \qquad (A.2)$$

The Action-Reaction equation (2.15) and (A.2) can be solved together to find expressions for both velocities.

$$v_m = -\frac{(\rho_m - \rho_f)}{c}\phi^2(1 - \phi)g + \Gamma\frac{(\rho_m - \rho_f)}{\rho_m \rho_f}z, \qquad (A.3)$$

$$v_f = \frac{(\rho_m - \rho_f)}{c}\phi(1 - \phi)^2 g + \Gamma\frac{(\rho_m - \rho_f)}{\rho_m \rho_f}z, \qquad (A.4)$$

A.2 Benchmarking the Coupled Crust-Ocean Model

Benchmarking of this model occurs in two steps. The model presented here is a moving boundary problem coupling both crustal and multiphase ocean dynamics. Thus, the first step is benchmarking the model of Triton's crust. The second step focuses on benchmarking a multiphase ocean.

A.2.1 A Purely Conductive Lid

Within this model, the crust experiences one main additional source of heating - tidal dissipation. For the purpose of benchmarking, this heat source is eliminated such that the crust becomes a purely conductive lid. As with the original model, it is assumed that Triton's crust is entirely solid. The evolution of the conductive lid is evaluated over a time scale of 4.5 Gyr and assumes no ocean exists within Triton's interior. Therefore, the base of the solid crust is assumed to extend to the depth of the core. The temperature at the base of the crust is held at a reference solidus temperature for an ammonia-water system ('reference' implies atmospheric pressure) for simplification.

Transient and Steady State Thermal Boundary Layers

If we assume the crust to be a purely conductive thermal boundary layer, approximately spanning the depth to Triton's core h_c, then we would expect the crust to cool according to the energy conservation equation such that:

$$\rho c_p \frac{\partial T_c}{\partial t} = k \frac{\partial^2 T_c}{\partial z^2} \tag{A.5}$$

where T_c is the potential temperature of the crust, t is time, ρ is density of the crust, c_p is specific heat, k is thermal conductivity, and z is depth.

If we assume steady state conditions, then we can simplify equation (A.5) to

$$0 = \frac{d^2 T_c}{dz^2} \tag{A.6}$$

The surface temperature T_{surf} of Triton is approximately 38 K (at $z = 0$ km). If we approximate the temperature at the base of the crust, at a depth h_c, to be equivalent to the solidus temperature T_{sol} of a simple ammonia-water system, then a steady state thermal profile of Triton's interior can be prescribed by

$$T_c = \left(\frac{T_{sol} - T_{surf}}{h_c} \right) z + T_{surf} \tag{A.7}$$
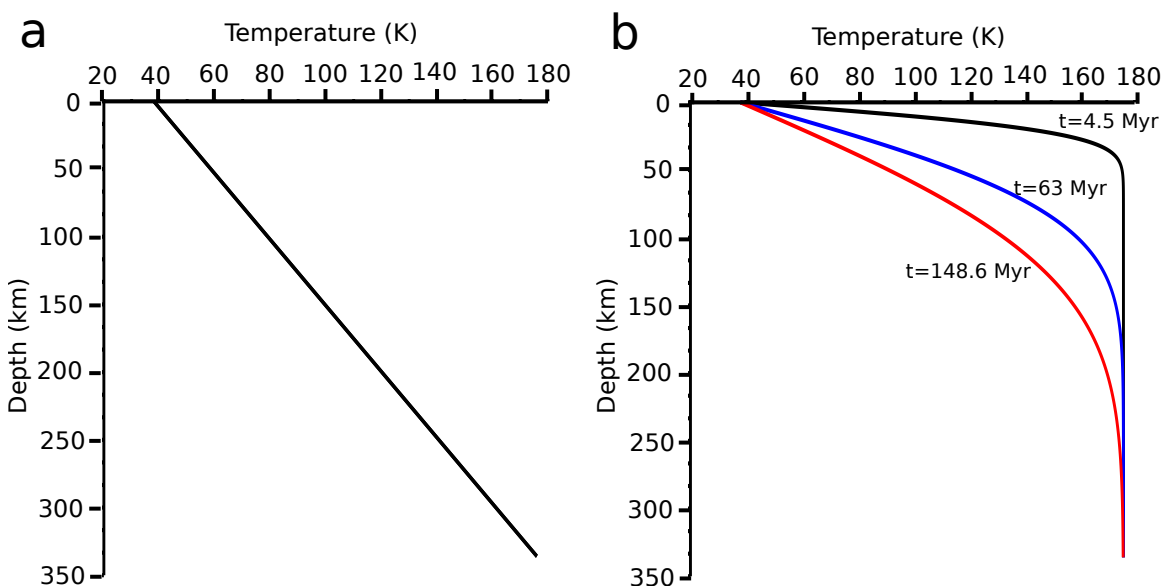
Figure A.1: **Crust Benchmark: Analytical Solution** - (a) The thermal state of Triton's crust is modeled given steady state conditions. (b) The thermal state of Triton's crust is modeled by evaluating Triton's thermal boundary layer as a semi-infinite half space. Each curve represents a geotherm at one instant of Triton's evolution: black is earlier (4.5 Myr), blue is about 63 Myr, and red is Triton at 148.6 Myr.

Figure A.1a shows the steady state thermal profile anticipated given these assumptions. For a transient conductive lid, however, we can model equation (A.5) as a semi infinite half space and assume instantaneous cooling. In this case, we assume that the temperature within the lid is initially equivalent to T_{sol}. A thermal profile can then be evaluated by

$$T_c = T_{sol} + (T_{surf} - T_{sol}) \left(1 - erf \left(\frac{z}{2 \left(\frac{kt}{\rho c_p} \right)^{0.5}} \right) \right) \tag{A.8}$$

Figure A.1b demonstrates a geotherm evaluated for 3 different scenarios. The first scenario occurs at an earlier stage of Triton's evolution, approximately 4.50 Myr. The second scenario represents a profile at 63.06 Myr. The final scenario represents Triton's profile after 148.6 Myr.

Finite Volume Discretization of a Purely Conductive Lid

For comparison to the previous solution, here we evaluate the equation for a purely conductive lid using finite volume discretization. Equation (A.5) is discretized to the form:

$$T_i^{n+1} = T_i^n + \frac{k}{\rho c_p} \frac{T_{i+1}^n - 2T_i^n + T_{i-1}^n}{dz^2} \tag{A.9}$$

where n denotes time iteration and i denotes spatial distribution.

After altering the pre-existing coupled crust-multiphase ocean code so that it focuses solely on the thermal evolution of a crust of constant thickness without any input from a multiphase ocean, we can use equation (A.9) to describe the crust's evolution. For comparison to the semi infinite half space model, we prescribe the initial condition such that the temperature of the lid is equal to the solidus temperature at $t = 0$. At $z = 0$, for $t > 0$, temperature is held at 0, which is an approximation of Triton's surface temperature. At the base of Triton's crust, the temperature is held at the solidus temperature.

The governing equation can be nondimensionalized using the following scheme:

$$T = T^* T_0$$

$$t = t^* \frac{H}{V}$$

$$v = v^* V$$

$$z = z^* H$$

$$H = \frac{\rho_f T_o \Delta S^2}{\Delta \rho g c_p} l \tag{A.10}$$

v is dimensional velocity, whereas V is nondimensional velocity. ρ_f is the fluid density within an ocean layer, ΔS is the change in entropy, $\Delta \rho$ is the difference in density between solid and liquid phases, and l is a scale factor to ensure that the lengthscale is comparable to the depth of Triton's icy layer. Using this scheme and dropping the nondimensional asterisk notation, Equation (A.9) becomes

$$T_i^{n+1} = T_i^n + \frac{k}{\rho c_p V H} \frac{T_{i+1}^n - 2T_i^n + T_{i-1}^n}{dz^2} \tag{A.11}$$

Figure A.2 shows the evolution of the crust's thermal profile calculated using this finite volume model in comparison to the analytical solution supplied by the transient semi infinite half space model.

Error Analysis

For comparison we show a closer look at the Transient Half Space Model solution relative to the Finite Volume Model solution in figure A.2, with depth ranging up to the thickness of Triton's lid. Each pair of curves are calculated given the same amount of elapsed time during Triton's history. We can calculate the difference, or error, between the numerical solution, T_{num}, and the exact solution, T_{exact}, simply by:

$$T_{num} - T_{exact} = \epsilon \tag{A.12}$$
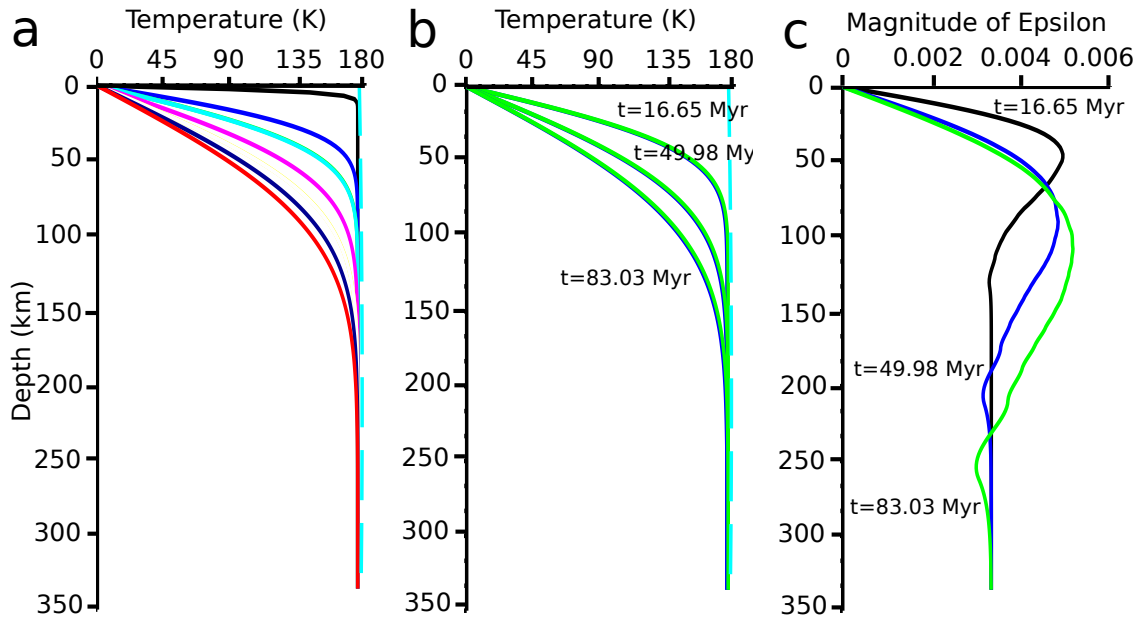
Figure A.2: **Finite Volume Discretization of Crust** - (a) The thermal state of Triton's crust is modeled by evaluating Triton's crust as a purely conductive lid and using finite volume discretization. Each curve represents a geotherm at one instant of Triton's evolution ranging from earlier (black) to later (red).(b) Here, we show a comparison of the exact solution determined by the half space cooling model (green) and the numerical solution determined using finite volume discretization (blue). Each pair is determined for the same time interval: 16.65 Myr, 49.98 Myr, 83.03 Myr. Each model uses a grid of 150 points. (c) Here, we show the difference between the exact solution and the numerical solution for each of the three pairs shown in (b) as a function of depth. Each curve represents one of the three time intervals: 16.65 Myr(black), 49.98 Myr (blue), 83.03 Myr (green).
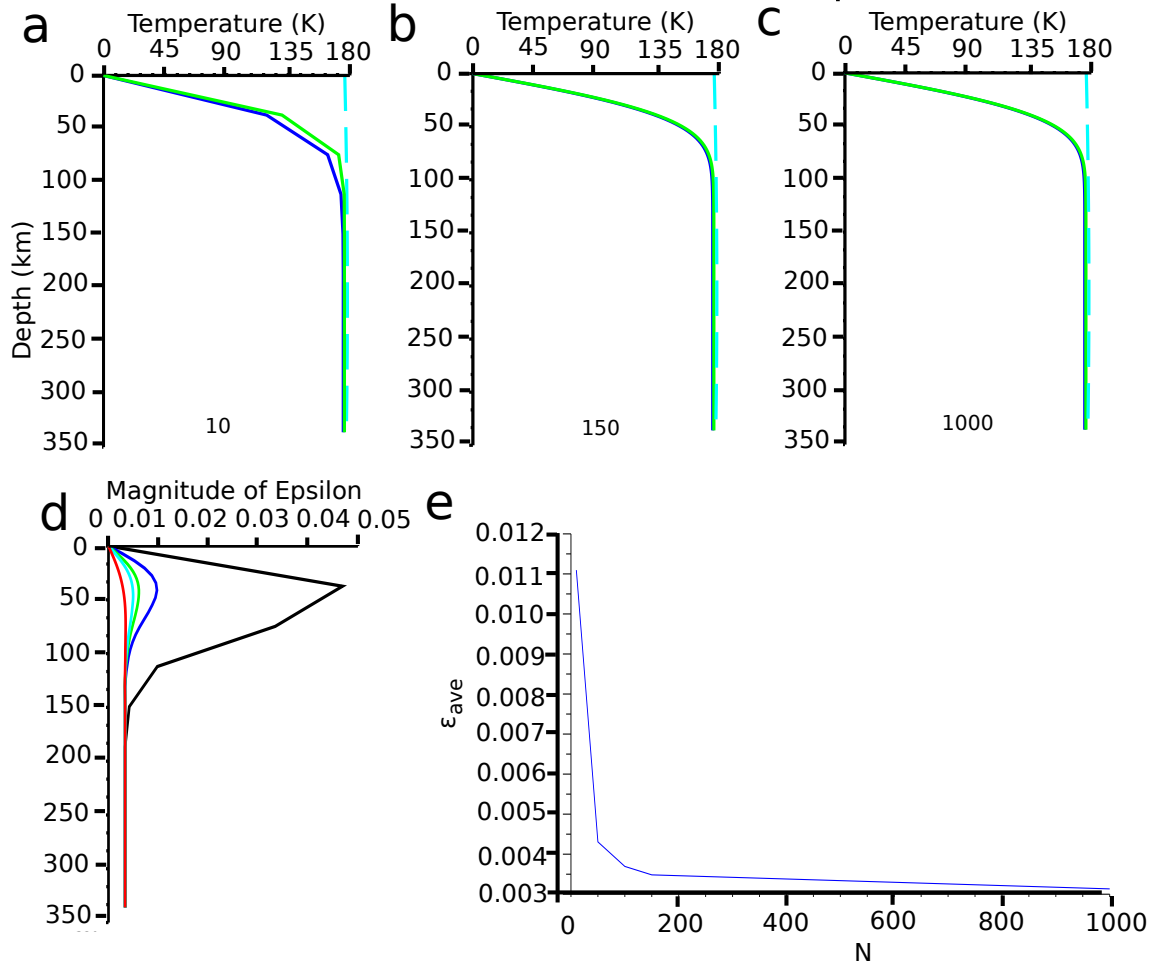
Figure A.3: **Minimizing Error** - (a)-(c)Here, we show the difference between the exact solution and the numerical solution for various grid sizes as a function of depth. Each pair shows results given a different grid size: 10, 150, and 1000. Grid sizes larger than 50 or 100 show very similar results. (d) Here, we show the difference between the exact solution and the numerical solution for various grid sizes as a function of depth. Each curve represents a different grid size: 10, 50, 100, 150, 1000. Error between solution is minimal amongst the largest grid sizes shown. (e) The average error between solutions can be shown to decrease as we increase the number of points distributed throughout the crust.

Figure A.2 shows the difference between the two solutions at each time interval, which appears to be minimal. Thus far, these solutions have been shown given a grid size comprising 150 points throughout the length of the crust. If we refine the grid by increasing the number of point, we may ultimately decrease error between solutions. Figure A.3 shows solutions for various grid sizes. The numerical solution appears to

become more similar to the exact solution with increasing grad size. However, the difference in error is minimal amongst the largest grid sizes shown. In Figure A.3, we see the error between solutions plotted for varying grid sizes, ranging from 10 to 1000 points over the entire crust. We can calculate the average error through:

$$|\bar{\epsilon}| = \frac{\sum_{i=1}^{N} |\bar{\epsilon}|}{N} \tag{A.13}$$

From Figure A.3, we can see that this error does decrease with grid size refinement.

Error within solution may also result from time stepping. Within the models shown here so far, we rely on a constant time step dt of 10^{-4}. If we rely on some form of adaptive time stepping, we can add constraints on the error within these calculations. In this model, we rely on the Courant Stability Criterion to determine appropriate time steps for constraining error. Figure A.4 shows a comparison between the exact solution for a grid size of 150 and the numerical solution for the same grid size, but incorporating an adaptive time step, reducing dt to the order of 10^{-5}. In figure A.4, it becomes apparent that the magnitude of error does not vary much given this change.

A.2.2 Multiphase Ocean Dynamics

The second step in benchmarking this model focuses on the multiphase ocean. Triton's subsurface ocean comprises two phases - fluid and solid - the composition of which are not well known. The coupled finite volume model evaluates temperature, melt distribution, and motion of phases as crystallization proceeds. The crust benchmark indicates that the model can evaluate thermal evolution, but how can the multiphase ocean model be further evaluated? Testing the validity of the model with regards to calculations of velocities of phases independent of temperature and variable melt fraction provides a second benchmark for the ocean model.

A study by Ricard et al. (2001), formulating a model intended to evaluate simple
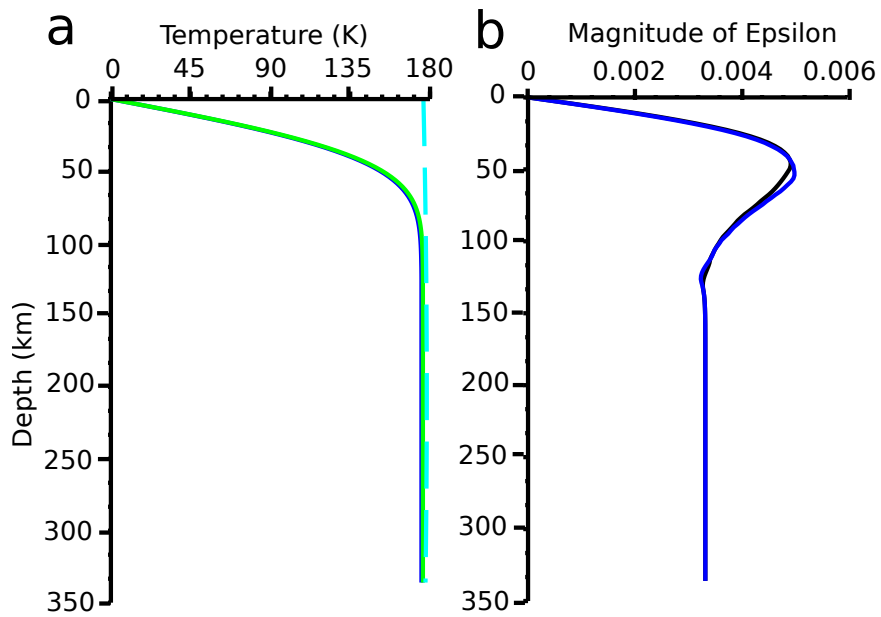
Figure A.4: **Comparison: Varying dt in FVM** -(a) Here, we show a comparison of the exact solution determined by the half space cooling model (green) and the numerical solution determined using finite volume discretization (blue) for given adaptive time stepping. Each model uses a grid of 150 points. (b) Here, we show the difference between the exact solution and the numerical solution as a function of depth for a FVM model using a constant dt of 10^{-4} (black) and a FVM model using adaptive time-stepping (blue).

compaction, is used to evaluate the velocities of both liquid and solid phases within a 1-D melting column. Within their model, the authors consider a layer of given thickness l_0 with a constant melt fraction ϕ_0 with depth. They assume that a piston resides at the top of the layer such that, when compressed, the solid matrix undergoes compaction while melt is expelled through the top of the piston.

From the conservation equation, a relationship between melt and matrix may be described by

$$\phi v_f + (1 - \phi) v_m = 0 \tag{A.14}$$

where ϕ is melt fraction, v_f is fluid velocity, and v_m is matrix velocity. The action-reaction equation is derived as:

$$-\phi(1-\phi)[\nabla \Delta P + \Delta \rho g z] + \nabla \cdot [\phi(1-\phi)\Delta \underline{\tau}] - \underline{\bar{\tau}} \cdot \nabla \phi - c \Delta v = 0 \tag{A.15}$$

where ΔP is change in pressure between phases, $\Delta \rho$ is change in matrix and melt density, g is gravitational acceleration, z is depth, $\Delta \underline{\tau}$ is difference in stress, $\underline{\bar{\tau}}$ is average stress, c is the interaction coefficient, and Δv is the difference in velocities.

From Navier-Stokes equations, the pressure jump within the system is then derived as:

$$\Delta P + \sigma \frac{d\alpha}{d\phi} = -K_0 \frac{(\mu_m + \mu_f)}{\phi(1-\phi)} \nabla \cdot [\phi(1-\phi)(v_m - v_f)] \tag{A.16}$$

where σ is surface tension between the phases, α is area of interface per volume, K_0 is a constant regarding surface of the interface, and μ_m and μ_f are matrix and melt viscosities respectively.

Within their study, Ricard et al. (2001) make the following simplifying assumptions: $g = 0$ and $\rho_m = \rho_f$ to avoid buoyancy effects; $\sigma = 0$ such that surface tension

can be ignored as well; $\mu_f \ll \mu_m$ to eliminate viscous stress. Combining Equations (A.14) through (A.16), finds

$$\phi^2 \delta_m^2 \left(\kappa \frac{(1 - \phi)}{\phi} + (1 - \phi) \right) \frac{\partial^2 v_m}{\partial z^2} - v_m = 0 \tag{A.17}$$

where δ_m is the compaction length equivalent to $\sqrt{\frac{4\mu_m}{3c}}$, and $\kappa = 3K_0/4$. If we assume $\kappa = 1$, we may further simplify Equation (A.17) to the form

$$\delta_m^2 \phi(1 - \phi^2) \frac{\partial^2 v_m}{\partial z^2} - v_m = 0 \tag{A.18}$$

The velocity of each phase within the layer is solved given two boundary conditions. At the top of the layer, $z = l_0$, v_m is kept constant at $-v_0$, the rate at which the piston compresses. The base of the layer, at $z = 0$, is considered an impermeable boundary, thus v_m is held at 0.

Nondimensionalization

Equation (A.18) can be nondimensionalized by velocity and depth as shown

$$v_m = v_0 v'_m$$

$$v_f = v_0 v'_f$$

$$z = \delta_m \sqrt{\phi_0(1 - \phi_0^2)} z' \tag{A.19}$$

Using Equation (A.19), Equation (A.18) can be rewritten as

$$\frac{\partial^2 v'_m}{\partial z'^2} - v'_m = 0 \tag{A.20}$$

Analytical Solution

As a standard linear ODE, the general solution to Equation (A.20) becomes

$$v'_m = c_1 \cosh z' + c_2 \sinh z' \qquad \text{(A.21)}$$

We may determine the coefficients within the solution using the given boundary conditions. The dimensionless boundary conditions at the bottom and top boundaries, respectively, are

$$z' = 0$$
$$v'_m = 0 \qquad \text{(A.22)}$$

and

$$z' = \frac{l_0}{\delta_m(\phi(1 - \phi^2))^{1/2}}$$
$$v'_m = -1 \qquad \text{(A.23)}$$

Thus, Equation (A.21) becomes

$$v'_m = -\frac{\sinh(z')}{\sinh(\frac{l_0}{h})} \qquad \text{(A.24)}$$

where

$$h = \delta_m(\phi(1 - \phi^2))^{1/2} \qquad \text{(A.25)}$$

We can determine the melt velocity given Equation (A.14).

$$v'_f = \frac{(1 - \phi)}{\phi} \frac{\sinh(z')}{\sinh(\frac{l_0}{h})} \qquad \text{(A.26)}$$

We first evaluate this solution given the parameters found within Ricard et al. (2001) for consistency. Within their study, $\mu_f = 10$Pa s, $\mu_m = 10^{18}$Pa s, $k_0 = 5 \times 10^{-10} m^2$, and ϕ_0 between 0.01 and 0.05. An estimate for l_0 is found provided that $(\frac{l_0}{\delta_m \phi_0})^2 = 0.1$ or 10. Therefore, l_0 is assumed to be approximately 130 m for a ratio equivalent to 0.1 and 1300 m for a ratio equivalent to 10. Figures A.5 (a) and (b) show the solutions consistent with their model. Reapplying this model towards Triton's ocean, it is necessary to alter some of these parameters. If we consider $\mu_f = 0.1$Pa s, $\mu_m = 10^{13}$Pa s, $k_0 = 5 \times 10^{-10} m^2$, and ϕ_0 between 0.01 and 0.05, using their constraints, we find the thickness of the layer l_0 to be approximately 4.1 m or 41 m respectively, several orders of magnitude smaller than an ocean on Triton. However, if we rely on the relationship used by Ricard et al. (2001) to constrain layer thickness, the solutions become identical with that of Figures A.5 (a) and (b). As depth and velocity are normalized to l_0 and v_m, identical solutions are ideal. As ϕ_0 increases, this relationship shows a decrease in the maximum melt velocity, indicated in Figures A.5 (e) and (f).

Numerical Solution

For comparison to the analytical solution, we can substitute the new equations describing our ocean layer into the main finite volume model. To do so, we must first discretize Equation (A.18) using a finite differencing scheme.

$$\frac{1}{\Delta z'^2}[v_m'^{i-1} - 2v_m'^i + v_m'^{i+1}] - v_m'^i = 0 \qquad (A.27)$$

where i denotes spatial variation. We can rewrite this equation in preparation for tridiagonalization:

$$v_m'^{i-1} - \left(2 + \Delta z'^2\right) v_m'^i + v_m'^{i+1} = 0 \qquad (A.28)$$
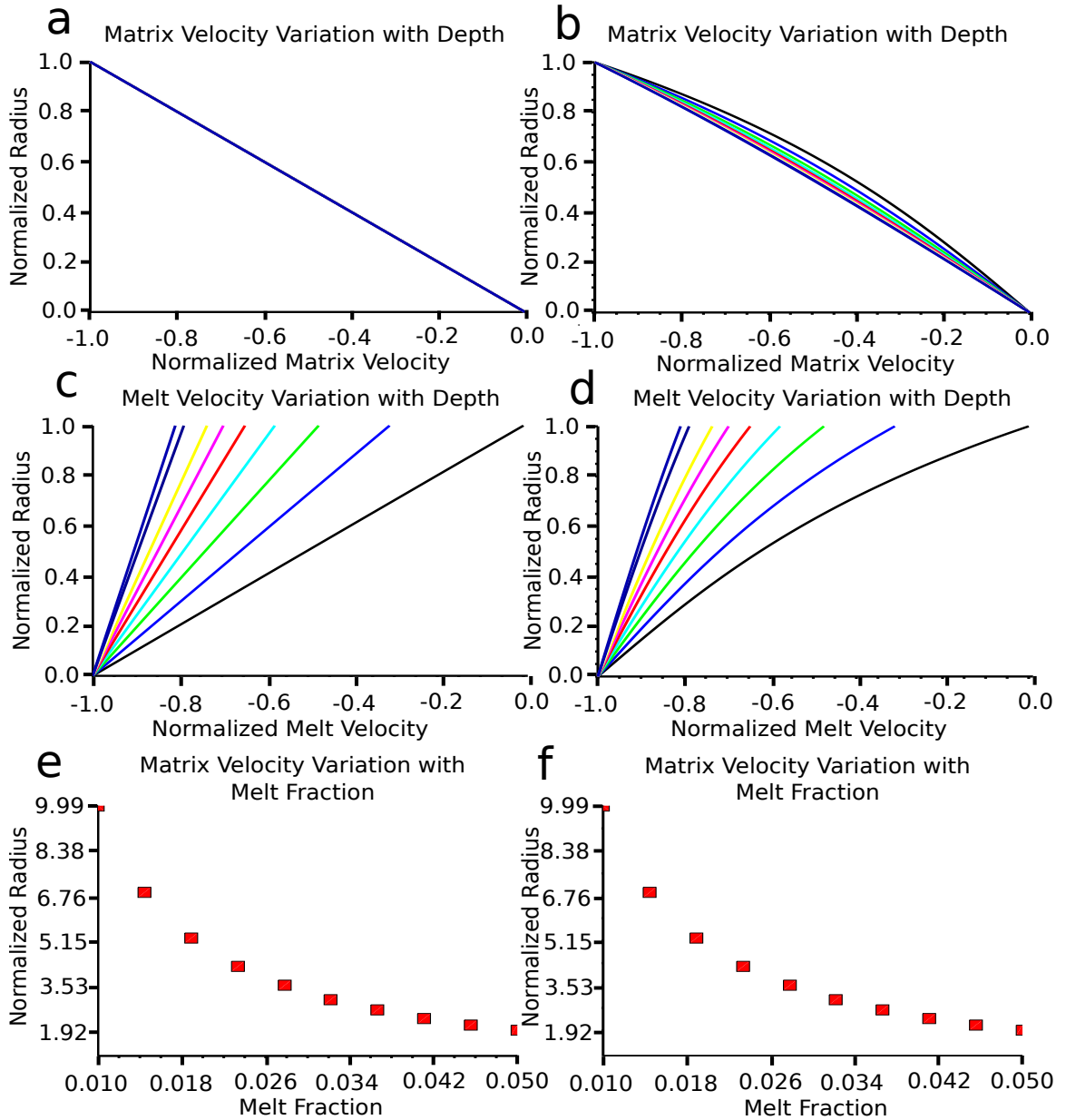
Figure A.5: **Variation of Velocity with Depth** - (a)-(b) Using the same method prescribed by Ricard et al. (2001), here we evaluate the normalized matrix velocity given parameters for Triton. Both velocity and depth are normalized by v_0 and l_0. Plot a: $(\frac{l_0}{\delta_m \phi_0}) = 0.1$; Plot b: $(\frac{l_0}{\delta_m \phi_0}) = 10$. (c)-(d) Melt velocity here has been determined relative to matrix velocity. Each color represents a distinct ϕ_0, with black representing the smallest melt fraction. Melt fraction increases from right to left. Both velocity and depth are normalized by v_0 and l_0. Plot c: $(\frac{l_0}{\delta_m \phi_0}) = 0.1$; Plot d: $(\frac{l_0}{\delta_m \phi_0}) = 10$ (e)-(f) Here, the maximum melt velocity is plotted as a function of ϕ_0. Plot e: $(\frac{l_0}{\delta_m \phi_0}) = 0.1$; Plot f: $(\frac{l_0}{\delta_m \phi_0}) = 10$

Claiming each coefficient as constant a_i, b_i, or c_i in order, we can now solve the system of equations as

$$Av_m = r$$

where A is the tridiagonal matrix of coefficients, v_m is the matrix velocity array to be solved, and r is an array of zeros given homogeneity of the solution.

$$A = \begin{bmatrix} b_1 & c_1 & & & & & \\ a_2 & b_2 & c_2 & & & & \\ & a_3 & b_3 & c_3 & & & \\ & & a_4 & b_4 & c_4 & & \\ & & & \cdots & \cdots & \cdots & \\ & & & & & a_n & b_n \end{bmatrix} \tag{A.29}$$

$$v_m = \begin{bmatrix} v_m^1 \\ v_m^2 \\ v_m^3 \\ v_m^4 \\ \cdots \\ v_m^n \end{bmatrix} \tag{A.30}$$

$$r = \begin{bmatrix} r^1 \\ r^2 \\ r^3 \\ r^4 \\ \cdots \\ r^n \end{bmatrix} \tag{A.31}$$

Using a form of Gauss elimination we can solve for matrix velocity. Figure A.6

illustrates a comparison between the analytical and numerical solutions determined here for matrix velocity. In this model, ϕ_0 is set to 0.1 and l_0 is determined to be approximately 8.164966 m in order to keep $\left(\frac{l_0}{\delta_m \phi_0}\right) = 0.1$. We can see the error between these solutions plotted within Figure A.6, as determined using similar methods to the crust benchmarking. Figure A.6 illustrates the comparison between melt velocity solutions as well.
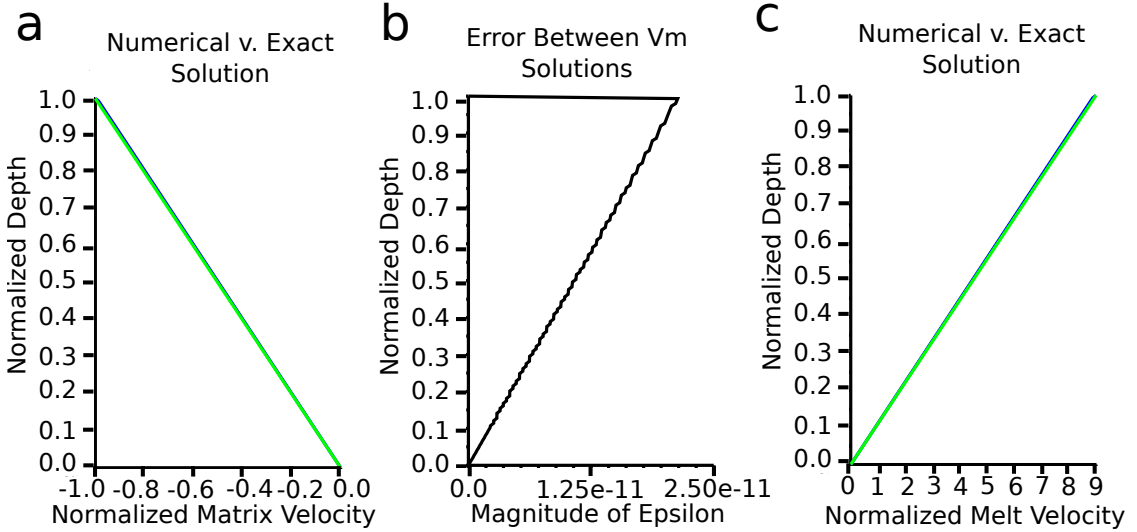

Figure A.6: **Analytical v. Numerical** V_m - (a) This plot illustrates a comparison between the analytical solution for v_m and the numerical solution for v_m for an initial melt fraction constant with depth - $\phi_0 = 0.1$. (b)The error between solutions shown in (a) is plotted as a function of depth. Error is relatively small. (c) Additionally, a comparison between the analytical solution for v_f and the numerical solution for v_f for $\phi_0 = 0.1$ is computed as well.

We further evaluate error between solutions by adjusting grid size, as performed with prior crust benchmarking calculations. Error ϵ between analytical and numerical solutions are determined using

$$v_{num} - v_{exact} = \epsilon \qquad (A.32)$$

We evaluate matrix and melt velocity for grids spanning 10, 50, 100, 150, 250, 500, and 1000 nodes. The results are displayed within Figures A.7 (a) and (b). The error between the numerical and analytical matrix velocity solutions is displayed more

clearly within Figure A.7 (c). Average error is determined using Equation (A.13). The average error within the solutions decreases with increasing grid size, as shown in Figure A.7 (d).

A.2.3 Benchmarking the Stefan Problem

This section provides some numerical benchmarks for a standard example of the Stefan problem. The governing nondimensional equations are

$$\frac{\partial T}{\partial t} = \frac{\partial^2 T}{\partial z^2}, 0 \leq z \leq h(t), t \geq 0, \tag{A.33}$$

subject to the boundary conditions,

$$T(z = 0, t) = 1, T(z = h(t), t) = 0, \tag{A.34}$$

and the initial condition

$$T(z, 0) = 0. \tag{A.35}$$

Also,

$$\frac{\mathrm{d}h}{\mathrm{d}t} = -St \left(\frac{\partial T}{\partial z} \right)_{z=h}, \tag{A.36}$$

subject to the initial condition $h(0) = 0$. Notice the difference in sign between (A.36) and (2.21) arising from the change in the prescription of the boundary conditions. In this work, we follow the BIM-based technique suggested by *Mitchell and Vynnycky* (2009). The following table contains comparison between our results, analytical values, and BIM values obtained by *Caldwell and Kwan* (2004). The exact solution to this problem is given by,

$$T(z, t) = 1 - \frac{\mathrm{erf}\left(z/(2\sqrt{t})\right)}{\mathrm{erf}(\lambda)}, \tag{A.37}$$

Time	This work	Exact	*Caldwell and Kwan* (2004)
0.5	0.43837	0.43334	0.43375
1.0	0.62024	0.61284	0.61318
1.5	0.75976	0.75057	0.75088
2.0	0.87736	0.86669	0.86697

Table A.1: **Numerical Benchmark for the Stefan problem**

where λ is a solution to the transcendental equation,

$$\sqrt{\pi}\lambda \exp\left(\lambda^2\right)\mathrm{erf}(\lambda) = St. \tag{A.38}$$

We benchmark our solutions for $St = 0.2$ (corresponding to $\lambda = 0.32$), for a grid size of 100 and time step $\Delta t = 0.001$, against this analytical solution and the results of *Caldwell and Kwan* (2004). The comparative results are presented in Table A.1.
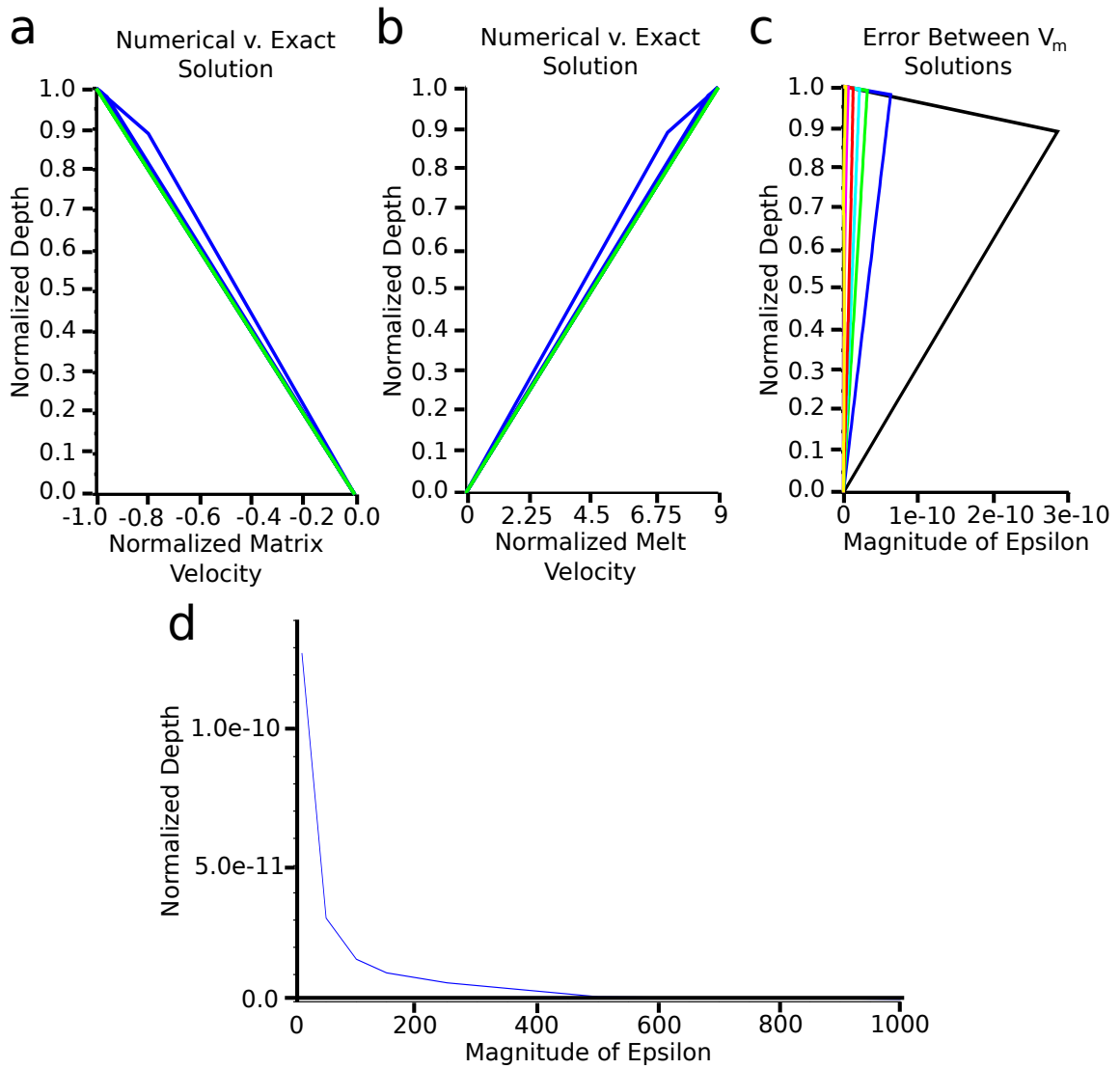
Figure A.7: V_m **Error: Varying Grid Size** - (a) Here, we show the error between v_m solutions for several grid sizes. The green line represents the analytical solution; blue lines represent numerical solutions. (b)Here, we show the error between v_f solutions for several grid sizes. The green line represents the analytical solution; blue lines represent numerical solutions. (c)Plot of the error between v_m solutions as a function of depth. Each color curve represents a different grid size. Node size increases right to left. (d) Average error for each grid size is shown, emphasizing the decrease in error with increasing grid size. However, grid sizes larger than 150 show minimal variation.

Bibliography

Abe, Y., Thermal and chemical evolution of the terrestrial magma ocean., *Physics of the Earth and Planetary Interiors*, *100*, 27–39, 1997.

Agnor, C. B., and D. P. Hamilton, Neptune's capture of its moon triton in a binary-planet gravitational encounter, *Nature*, *441*, 192–94, 2006.

Alterman, Z., H. Jarosch, and C. Pekeris, Oscillations of the Earth., *Proc. R. Soc. London A*, *252*, 80–95, 1959.

Bauer, J. M., B. J. Buratti, J.-Y. Li, J. A. Mosher, M. D. Hicks, B. E. Schmidt, and J. D. Goguen, Direct detection of seasonal changes on triton with hubble space telescope, *The Astrophysical Journal Letters*, *723*, 2011.

Brown, R. H., and D. P. Cruikshank, Determination of the composition and state of icy surfaces in the outer solar system, *Annual Reviews of Earth and Planetary Science*, *25*, 243–77, 1997.

Brown, R. H., and R. L. Kirk, Coupling of volatile transport and internal heat flow on triton., *Journal of Geophysical Research*, *99*, 1965–981, 1994.

Caldwell, J., and Y. Kwan, Numerical methods for one-dimensional Stefan problems, *COMMUNICATIONS IN NUMERICAL METHODS IN ENGINEERING*, *20*, 535–545, 2004.

Choukroun, M., and O. Grasset, Thermodynamic model for water and high-pressure ices up to 2.2 gpa and down to the metastable domain, *Journal of Chemical Physics*, *127*, 2007.

Choukroun, M., and O. Grasset, Thermodynamic data and modeling of the water and ammonia-water phase diagrams up to 2.2 gpa for planetary geophysics, *Journal of Chemical Physics*, *133*, 2010.

Croft, S., J. Lunine, and J. Kargel, Equation of state of ammonia-water liquid: Derivation and planetological applications, *Icarus*, *73*, 1988.

Fortes, A., I. Wood, J. Brodholt, M. Alfredsson, L. Vocadlo, G. McGrady, and K. Knight, A high-resolution neutron powder diffraction study of ammonia dihydrate (nd3 2d2o) phase i, *Journal of Chemical Physics*, *119*, 2003.

Grossmann, S., and D. Lohse, Scaling in thermal convection: a unifying theory, *Journal of Fluid Mechanics*, *407*, 27–56, 2000.

Grossmann, S., and D. Lohse, Multiple scaling in the ultimate regime of thermal convection, *Physics of Fluids*, *23*, 2011.

Hogenboom, D., J. Kargel, G. Consolmagno, L. L. T.C. Holden, and M. Buyy-ounouski, The ammonia-water system and the chemical differentiation of icy satellites, *Icarus*, *128*, 171–80, 1997.

Hussmann, H., and T. Spohn, Thermal-orbital evolution of io and europa, *Icarus*, *171*, 391–410, 2004.

Hussmann, H., F. Sohl, and T. Spohn, Subsurface oceans and deep interiors of medium-sized outer planet satellites and large trans-neptunian objects, *Icarus*, *185*, 258–73, 2006.

Kargel, J., Cryovolcanism on the icy satellites, *Earth, Moon, and Planets*, *67*, 101–113, 1995.

McKinnon, W. B., and R. L. Kirk, *Encyclopedia of the Solar System*, chap. Triton, pp. 483–502, Academic Press, 2007.

McKinnon, W. B., and A. C. Leith, Gas drag and the orbital evolution of a captured triton, *Icarus*, *118*, 392–413, 1995.

Mitchell, S. L., and M. Vynnycky, Finite-difference methods with increased accuracy and correct initialization for one-dimensional Stefan problems, *APPLIED MATHEMATICS AND COMPUTATION*, *215*, 1609–1621, 2009, International Workshop on Physics and Computation, Vienna, AUSTRIA, AUG 25-28, 2008.

Press, W. H., S. A. Teukolsky, and W. T. Vetterling, *Numerical Recipes in Fortran 77 Vol.1: The Art of Scientific Computing*, vol. 1, pp. 704–16, 2 ed., Cambridge UP, New York, 1992.

Prockter, L. M., F. Nimmo, and R. Pappalardo, A shear heating origin for ridges on triton, *Geophysical Research Letters*, *32*, 2005.

Roberts, J. H., and F. Nimmo, Tidal heating and the long-term stability of a subsurface ocean on enceladus, *Icarus*, *194*, 675–689, 2008.

Ross, M. N., and G. Schubert, The coupled orbital and thermal evolution of triton, *Geophysical Research Letter*, *17*, 1749–752, 1990.

Ruiz, J., Heat flow and depth to a possible internal ocean on triton, *Icarus*, *166*, 436–39, 2003.

Sabadini, R., and B. Vermeersen, *Global Dynamics of the Earth: Applications of Normal Mode Relaxation Theory to Solid-Earth Geophysics*, Kluwer Academic Publishers, Dordrecht, the Netherlands, 2004.

Schenk, P., and M. Jackson, Diapirism on triton: A record of crustal layering and instability, *Geology*, *21*, 299–302, 1993.

Schenk, P. M., and K. Zahnle, On the negligible surface age of triton, *Icarus*, *192*, 135–49, 2007.

Schubert, G., D. L. Turcotte, and P. Olson, *Mantle Convection in the Earth and Planets*, Cambridge University Press, Cambridge, 2000.

Shraiman, B. I., and E. D. Siggia, Heat transport in high-rayleigh-number convection, *Physical Review A*, *42*, 1990.

Solomatov, V., Fluid dynamics of a terrestrial magma ocean, in *Origin of the Earth and Moon*, pp. 323–38, University of Arizona P, 2000.

Solomatov, V., Magma oceans and primordial mantle differentiation, pp. 91–119, Elsevier B.V., 2007.

Solomatov, V. S., and D. J. Stevenson, Nonfractional crystallization of a terrestrial magma ocean, *Journal of Geophysical Research*, *98*, 5391–406, 1993a.

Solomatov, V. S., and D. J. Stevenson, Suspension in convective layers and style of differentiation of a terrestrial magma ocean., *Journal of Geophysical Research*, *98*, 5375–390, 1993b.

Sramek, O., Y. Ricard, and D. Bercovici, Simultaneous melting and compaction in deformable two-phase media, *Geophys. J. Int.*, *168*, 964–982, 2007.

Tobie, G., A. Mocquet, and C. Sotin, Tidal dissipation within large icy satellites: Applications to europa and titan, *Icarus*, *177*, 534–549, 2005.